DORA: Exploring outlier representations in Deep Neural Networks

Anonymous authors
Paper under double-blind review

Abstract

Deep Neural Networks (DNNs) draw their power from the representations they learn. However, while being incredibly effective in learning complex abstractions, they are susceptible to learning malicious concepts, due to the spurious correlations inherent in the training data. So far, existing methods for uncovering such artifactual behavior in trained models focus on finding artifacts in the input data, which requires both availability of a data set and human supervision. In this paper, we introduce DORA (Data-agnOstic Representation Analysis): the first *data-agnostic* framework for the analysis of the representation space of DNNs. We propose a novel distance measure between representations that utilizes self-explaining capabilities within the network itself without access to any data and quantitatively validate its alignment with human-defined semantic distances. We further demonstrate that this metric could be utilized for the detection of anomalous representations, which may bear a risk of learning unintended spurious concepts deviating from the desired decision-making policy. Finally, we demonstrate the practical utility of DORA by analyzing and identifying artifactual representations in widely popular Computer Vision models.

1 Introduction

The ability of Deep Neural Networks (DNNs) to perform complex tasks and achieve *state-of-the-art* results in various fields can be attributed to the rich and hierarchical representations that they learn from the input data Bengio et al. (2013). Far beyond the handcrafted features that were inductively constructed by humans on learning machines in classical Machine Learning methods Marr and Nishihara (1978); Jackson; Fogel and Sagi (1989), Deep Learning approaches exploit the network's freedom for representation learning, which, however, leads to a semantic opacity of learned abstractions. The rapid progress in representation learning only exacerbates the issue of interpretability, as modern DNNs are often trained in a self-supervised manner Jaiswal et al. (2020); LeCun and Misra (2021) and from a potentially limitless amount of data Brown et al. (2020); Bommasani et al. (2021), alleviating human control over the training dataset, and resulting in unpredictable decision-making strategies.

The increasing popularity of Deep Learning techniques across various fields, coupled with the difficulty of interpreting the decision-making processes of complex models, has led to the emergence of the field of Explainable AI (XAI) (e.g. Montavon et al. (2018); Samek et al. (2019); Xu et al. (2019); Gade et al. (2019); Rudin (2019); Samek et al. (2021)). Research within XAI has revealed that the internal representations that form the basis of DNNs are susceptible to learning harmful and undesired concepts, such as biases Guidotti et al. (2018); Jiang and Nachum (2020), Clever Hans (CH) effects Lapuschkin et al. (2019), and backdoors Anders et al. (2022). The learned artifactual concepts are often unnaturally and semantically distant from the relevant concepts within the dataset, such as watermarks in the PASCAL 2012 image classification task Lapuschkin et al. (2019), Chinese logographic watermarks in ImageNet dataset Li et al. (2022), colored band-aids in skin-cancer detection problem Anders et al. (2022) or tokens in a pneumonia detection problem Zech et al. (2018).

In order to improve understanding of the decision-making processes of complex machines and prevent the network from making biased or harmful decisions, it is crucial to identify the specific internal representations responsible for learning undesired concepts. In this work, we propose *DORA*[*] — the first data-agnostic framework allowing an automatic inspection of the representation space of Deep Neural Networks. DORA leverages the self-explanation capabilities of the networks, allowing for the approximation of the semantic distances between different learned representations, independent of the availability of the specific data used for training. By assuming that artificial representations, which deviate from the desired decision-making policy, are semantically distant from the relevant representations learned by the network, DORA allows the detection of potentially harmful representations that may lead to unintended learning outcomes. Additionally, DORA can be further used to identify and remove infected data points.

The primary contributions of this research are as follows:

- We introduce the data-agnostic DORA framework for analyzing the representation space of Deep Neural Networks (DNNs).
- We introduce the Extreme Activation (EA) distance between representations and demonstrate its alignment with human-defined semantic distances in controlled scenarios.
- We quantitatively evaluate the ability of the DORA framework to detect semantically anomalous representations in controlled scenarios.
- We demonstrate the application of DORA on popular Computer Vision models and show that in real-world applications, outlier representations may encode undesirable and harmful concepts.

2 Related Work

In order to address the concerns about the black-box nature of the complex learning machines Baehrens et al. (2010); Vidovic et al. (2015); Buhrmester et al. (2019); Samek et al. (2021), the field of *Explainable AI (XAI)* has emerged. While some recent research focuses on inducing the self-explaining capabilities through changes in the architecture and the learning process Gautam et al. (2022); Chen et al. (2018); Gautam et al. (2021), the majority of XAI methods (typically referred to as *post-hoc* explanation methods) are decoupled from the training procedure. A dichotomy of post-hoc explanation methods could be performed based on the notion of their explanations, i.e., the model behavior can be either explained on a *local* level, where the decision-making strategy of a system is explained for one particular input sample, or on a *global* data set level, where the aim is to explain the prediction strategy learned by the machine across the data set and investigate the purpose of its individual components in a universal fashion detached from single data points (similar to feature selection Guyon and Elisseeff (2003)).

Local explanation methods, often produce attribution maps, interpreting the prediction by attributing relevance scores to the features of the input signal, highlighting the influential characteristics that affected the prediction the most. Various methods, such as Layer-wise Relevance Propagation (LRP) Bach et al. (2015), GradCAM Selvaraju et al. (2019), Occlusion Zeiler and Fergus (2014), MFI Vidovic et al. (2016), Integrated Gradient Sundararajan et al. (2017), have proven effective in explaining DNNs Tjoa and Guan (2020) as well as Bayesian Neural Networks Bykov et al. (2021); Brown and Talbert (2022). To further boost the quality of interpretations, several enhancing techniques were introduced, such as SmoothGrad Smilkov et al. (2017); Omeiza et al. (2019), NoiseGrad and FusionGrad Bykov et al. (2022). Considerable attention also has been paid to analyzing and evaluating the quality of local explanation methods (e.g. Samek et al. (2016); Hedström et al. (2022); Guidotti (2021)). However, while the local explanation paradigm is incredibly powerful in transferring the understanding of the decision-making strategies for a particular data sample, it lacks the ability to provide an overall view of the inner processes of representations in a network.

Global explanation methods aim to interpret the general behavior of learning machines by investigating the role of particular components (e.g., neurons, channels, or output logits), which we refer to as representations. Existing methods mainly aim to connect internal representations to human understandable concepts, making

[*] PyTorch implementation of the proposed method could be found by the following link: `anonimyzed` .

the purpose and semantics of particular network sub-function transparent to humans. Methods such as Network Dissection Bau et al. (2017; 2018) and Compositional Explanations of Neurons Mu and Andreas (2020) aim to label representations with class labels from a given dataset, based on the intersection between the class relevant information provided by a binary mask information and the activation map of the representation, while the MILAN method generates a text-description of the representation by searching for a text string that maximizes the mutual information with the image regions in which the neuron is active Hernandez et al. (2021).

2.1 Activation-Maximisation methods

The family of Activation-Maximization (AM) Erhan et al. (2009) methods is designed for the global explanation of complex learning machines by identifying the input that maximally activates a particular neuron or layer in the network in order to visualize the features that have been learned by the neuron or layer. These signals, which we will refer to as Activation-Maximization Signals (AMS), could be either natural signals(n-AMS), found in a *data-aware* fashion by selecting a “real” example from an existing data corpus Borowski et al. (2020), or artificial (synthetic AMS or s-AMS), found in a *data-agnostic* mode by generating a synthetic input through optimization Erhan et al. (2009); Olah et al. (2017); Szegedy et al. (2013).

Modern machine learning models are often trained on closed-source or very large datasets, making it difficult to obtain a subset that fully represents the diversity of concepts that the model might potentially learn. If the corpus used for n-AMS selection does not include all potential concepts, the analysis of a concept by using this specific data set may be misleading as shown exemplarily in Figure 1, where analysis based solely on natural signals leads to erroneous conclusions about the learned concept due to the absence of the true concept in the dataset.

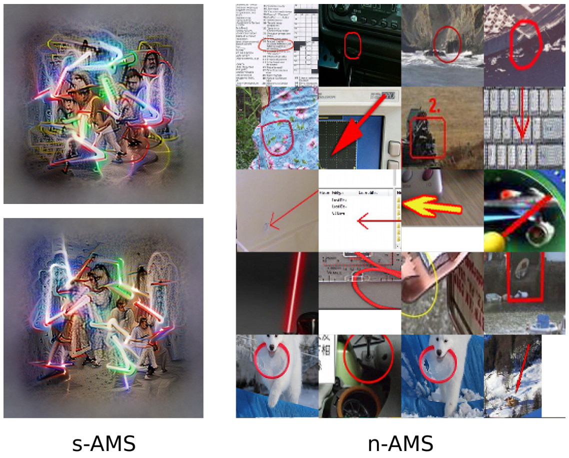

Figure 1: **Failing to explain“Star Wars” representation with n-AMS.** Comparison of the s-AMS (left) and n-AMS (right) collected from the ImageNet dataset for unit 744 in the last convolutional layer of the CLIP ResNet50 model. Due to the inaccessibility of the training dataset and lack of specific images due to copyright restrictions, n-AMS struggle to illustrate the concept of the “Star Wars” neuron. Illustrated signals were obtained from OpenAI Microscope.

In comparison to earlier synthetic AM methods, Feature Visualization (FV) Olah et al. (2017) performs optimization in the frequency domain by parametrizing the image with frequencies obtained from the Fourier transformation. This reduces adversarial noise in s-AMS (e.g. Erhan et al. (2009); Szegedy et al. (2013)) — improving the interpretability of the obtained signals. Additionally, the FV method applies multiple stochastic image transformations, such as jittering, rotating, or scaling, before each optimization step, as well as frequency penalization, which either explicitly penalizes the variance between neighboring pixels or applies bilateral filters on the input.

2.2 Spurious correlations

Deep Neural Networks are prone to learn spurious representations — patterns that are correlated with a target class on the training data but not inherently relevant to the learning problem Izmailov et al. (2022). Reliance on spurious features prevents the model from generalizing, which subsequently leads to poor performance on sub-groups of the data where the spurious correlation is absent (cf. Lapuschkin et al. (2016; 2019); Geirhos et al. (2020)). In Computer Vision, such behavior could be characterized by the reliance of the model on an image’s background Xiao et al. (2020), object textures Geirhos et al. (2018), or the presence of semantic artifacts in the training data Wallis and Buvat (2022); Lapuschkin et al. (2019); Geirhos et al. (2020); Anders et al. (2022). Artifacts can be added to the training data on purpose as Backdoor attacks Gu et al. (2017);

Tran et al. (2018), or emerge "naturally" and might persist unnoticed in the training corpus, resulting in *Clever Hans effects* Lapuschkin et al. (2019).

Recently, XAI methods have demonstrated their potential in revealing the underlying mechanisms of predictions made by models, particularly in the presence of artifacts such as Clever Hans or Backdoor artifacts. Spectral Relevance analysis (SpRAy) aims to provide a global explanation of the model by analyzing local explanations across the dataset and clustering them for manual inspection Lapuschkin et al. (2019). While successful in certain cases Schramowski et al. (2020), SpRAy requires a substantial amount of human supervision and may not detect artifacts that do not exhibit consistent shape and position in the original images. SpRAY-based Class Artifact Compensation Anders et al. (2022) method significantly reduced the need for human supervision and demonstrated its capability to effectively suppress the artifactual behavior of DNNs, significantly reducing a model's Clever Hans behavior.

2.3 Comparison of representations

The study of representation similarity in DNN architectures is a topic of active research. Many methods for comparing network representations have been applied to various architectures, including Neural Networks of varying width and depth Nguyen et al. (2020), Bayesian Neural Networks Grinwald et al. (2022), and Transformer Neural Networks Raghu et al. (2021). Some works Ramsay et al. (1984); Laakso (2000); Kornblith et al. (2019); Nguyen et al. (2022) argue that similarity should be based on the correlation of a distance measure applied to layer activations on training data. Other works Raghu et al. (2017); Morcos et al. (2018) compute similarity values by applying variants of Canonical Correlation Analysis (CCA) Hardoon et al. (2005); Bießmann et al. (2010) on activations or by calculating mutual information Li et al. (2015). However, these methods require the presence of training data.

3 DORA: Data-Agnostic Representation Analysis

In the following, we introduce the DORA (Data-agnostic Representation Analysis) framework for analyzing representation spaces of DNNs. DORA utilizes a data-independent distance measure, referred to as *Extreme-Activation* (EA) distance, which estimates the similarity between neural representations by analyzing the similarities of their s-AMS. DORA leverages the distance measure to produce a visualization of the representation space through a process of dimensionality reduction, referred to as the *representation atlas*, providing a comprehensive overview of the topological landscape of learned representations. Additionally, the framework enables the detection of outlier representations that may potentially contain representations with undesirable and anomalous concepts.

We define *neural representations* as functions that depict the computation graph, from input to the output of a specific neuron. Representations are a vital aspect of neural networks as they enable the network to extract and utilize relevant information from the input data, leading to precise predictions or classifications.

Definition 1 (Neural representation)**.** *We define a neural representation f as a real-valued function $f : \mathbb{D} \to \mathbb{R}$, mapping from the data domain $\mathbb{D}$ to the set of real numbers.*

In DNNs, neural representations are combined into layers — collections of individual neural representations that typically share the same computational architecture and learn abstractions of similar complexity. We define a layer F as a collection of k individual neural representations, and refer to it both as a set of functions and as a function itself, where the output vector is given by the activations of the individual representations within the layer:

$$F(x) = [f_1(x), ..., f_k(x)] : \mathbb{D} \longrightarrow \mathbb{R}^k.$$

3.1 Extreme-Activation distance

For a specific neural representation f, a synthetic activation-maximization signal s can be generated to visualize the concepts that maximize the function activation.

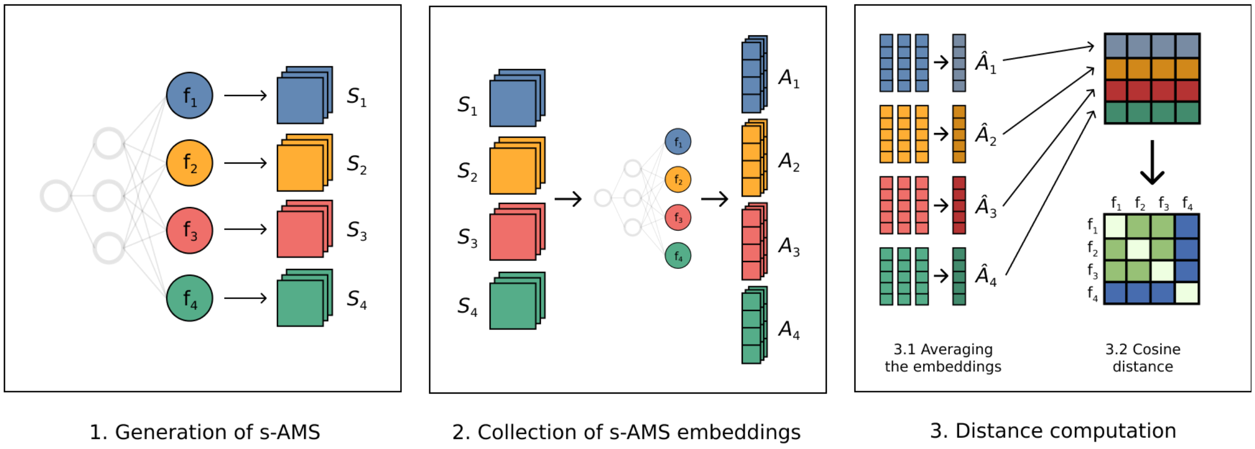

1. Generation of s-AMS

2. Collection of s-AMS embeddings

3. Distance computation

Figure 2: **Estimation of the (layer-wise) Extreme Activation Distance:** 1. Generating s-AMS for a set of neurons (left), 2. Collecting the embeddings of the generated s-AMS from Step 1 (middle), 3. Averaging the embedding vectors and computing the cosine similarity.

Definition 2. *Given a neural representation f, we define synthetic Activation-Maximization signal (s-AMS) s as a solution to the following optimization problem*

$$s = \arg\max_{x \in \mathcal{C}} f(x),$$

where $\mathcal{C}$ is a regularized input domain, specific to a particular implementation of the Activation-Maximization method.

In this paper, we employ the Feature Visualization method Olah et al. (2017) for s-AMS generation. The method has a wide set of adjustable hyperparameters including the number of optimization steps m applied to s-AMS generation. Activation-Maximisation methods are prone to finding only local solutions to the optimization problem, which can lead to indeterminacy due to the influence of different initial states of the parametrized signals. To address indeterminacy and multimodality Goh et al. (2021) (e.g., the ability of single representation to encode multiple concepts), we generate n s-AMS signals per representation for stability in calculated distances. The effect of these two parameters will be examined in the evaluation section.

Given a layer F containing k neural representations defined on the domain $\mathbb{D} \subset \mathbb{R}^d$, where d is the dimension of the input of the model, computation of Extreme-Activation distance could be summarized in three steps, as illustrated in Figure 2:

1. **Generation of s-AMS**

   For each neural representation $f_i \in F, \forall i \in [1, ...k]$, a collection of n s-AMS is generated:

   $$S_i = \left[s_i^1, ..., s_i^n\right], \forall i \in [1, ...k],$$

   where $s_i^t \subset \mathbb{R}^d$ is the t-th s-AMS sample for representation f_i. The parameter n controls the number of generated signals, which are generated non-deterministically.

2. **Collection of s-AMS embeddings**

   After s-AMS sets $S_i \subset \mathbb{R}^{n \times d}, \forall i \in [1, ..., k]$ are collected for all representations in F, signals are successively inferenced by the model, and their corresponding activations across representations in F are saved. For each set of s-AMS signals S_i we obtain a collection of vectors

   $$A_i = \left[F(s_i^1), ..., F(s_i^n)\right] \subset \mathbb{R}^{n \times k}, \forall i \in [1, ...k],$$

   where $F(s_i^t)$ correspond to the k-dimensional embedding of the $t - th$ s-AMS sample generated for representation f_i.

3. **Computing cosine similarity between average embeddings**

   Finally, for every representation $f_i \in F, \forall i \in [1, ...k]$, we average the embeddings, corresponding to the generated signals

   $$\hat{A}_i = \frac{1}{n}\sum_{t=1}^{n} F(s_i^t) \subset \mathbb{R}^k, \forall i \in [1, ..., k],$$

   resulting in a single embedding vector for each representation in F. The EA distance between two representations $f_i, f_j \subset F$ is then defined as the square root of the cosine distance between the k-dimensional vectors of the averaged embeddings:

   $$d_{EA}(f_i, f_j) = \frac{1}{\sqrt{2}}\sqrt{1 - \cos\left(\hat{A}_i, \hat{A}_j\right)},$$

   where $\cos(A, B)$ is the cosine similarity between vectors A and B.

The Extreme-Activation distance between two representations is determined by comparing the similarity of their s-AMS. If two representations encode semantically similar concepts, their s-AMS will likely be visually similar and illustrate similar concepts. For instance, the s-AMS generated by representations for cat and tiger detectors are expected to show a visual similarity due to inherent similarities between the classes, while the s-AMS generated by representations for cat and car detectors will likely be visually dissimilar. To quantify the similarity between s-AMS, our approach utilizes the network itself to generate embeddings of the signals across the layer being analyzed. Although the visual similarity between s-AMS could be evaluated using an external model, we refrain from this approach to maintain transparency and avoid introducing additional opaqueness from an external model. The collected embeddings are then compared using cosine similarity, where a cosine value close to 1 indicates that both representations share common activation-maximization concepts, whereas a cosine value close to 0 indicates that the two representations encode independent concepts. Since cosine similarity is not a distance metric, we apply a square root transformation to limit the resulting distance between 0 and 1, thereby ensuring that the EA distance measure satisfies the criteria of a proper distance metric.

Combining all the steps, Extreme-Activation distance could be formulated as follows:

Definition 3. *Let F be a layer with k neural representations and $f_i, f_j \in F$ be individual representations. The Extreme-Activation (EA) distance between f_i and f_q is given by:*

$$d_{EA}(f_i, f_j) = \frac{1}{\sqrt{2}}\sqrt{1 - \cos\left(\frac{1}{n}\sum_{t=1}^{n} F(s_i^t), \frac{1}{n}\sum_{t=1}^{n} F(s_j^t)\right)},$$

where $\left[s_i^1, ..., s_i^n\right]$ and $\left[s_j^1, ..., s_j^n\right]$ are collections of s-AMS for f_i and f_j, respectively, $\cos(A, B)$ *is the cosine similarity between vectors A and B, and n is the parameter of the method, controlling the number of generated s-AMS per representation.*

Pair-wise vs Layer-wise embeddings

In the EA distance, the embeddings of s-AMS signals are obtained from all representations in the layer F, implying that the distance between two representations $f_i, f_q \in F$ depends on how all the representations in F respond to their s-AMS. This approach, in which embeddings are collected across the entire layer, is referred to as *layer-wise* (l-w). An alternative approach would be to collect embeddings only from the representations for which the distance is being calculated, i.e. when computing the distance between f_i and f_q, embeddings $A_i, A_q \subset \mathbb{R}^{n\times 2}$ of s-AMS are collected only from the two representations themselves, independent of the other representations in the layer. This approach is referred to as *pair-wise* (p-w), and we compare both approaches in the evaluation section. Unless otherwise specified, the default DORA method uses layer-wise EA distance computation.

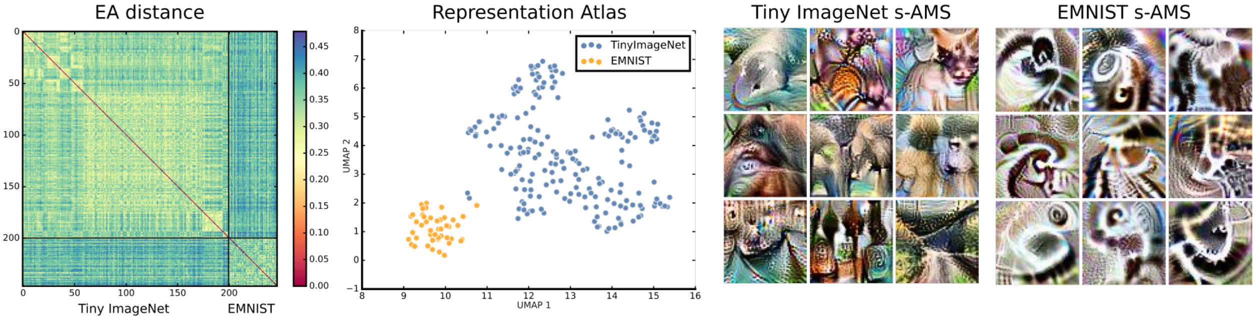

Figure 3: **Illustration of the performance of DORA on a toy example.** From left to right: EA distance metric between the output logits of the network trained on the combined dataset, UMAP visualization of the representational space, and s-AMS for Tiny ImageNet logits and for EMNIST logits. Visual differences between s-AMS for ImageNet and EMNIST classes can be observed and measured by the activations of the representations, resulting in a clear and visible cluster structure of the distance matrix.

3.2 Representation atlas and Outlier detection

The calculation of EA distances between the k neural representations in layer F results in a distance matrix $D \in \mathbb{R}^{k \times k}$. As shown in subsequent sections, this matrix effectively captures the semantic distance between the concepts encoded in the representations. Inspired by Carter et al. (2019), to visually examine the topological landscape of learned representations and identify clusters of semantically similar representations, we pass a pre-computed distance matrix to the UMAP dimensionality reduction algorithm McInnes et al. (2018) to output a two-dimensional map of the representation space, referred to as the *representation atlas*. By utilizing the distance matrix between representations, we can also identify outlier representations that deviate semantically from the majority. We further demonstrate in our analysis that such representations often learn unnatural and unintended concepts.

3.3 Toy experiment

To demonstrate the capabilities of our proposed framework, we conducted a simple toy experiment by training a ResNet18 He et al. (2016) network on a combination of two conceptually different datasets. The combined dataset comprised the Tiny Imagenet Le and Yang (2015), containing 200 ImageNet classes, and the EMNIST dataset Cohen et al. (2017), an extension of the MNIST dataset for handwritten letters containing 47 handwritten letters and numbers resulting in a total of 247 classes. EMNIST images were upsampled to the size of 3 × 64 × 64 pixels to match the size of images in Tiny ImageNet. After training on the combined dataset in the image classification task, we computed EA distances between the output logits. The results obtained by DORA are shown in Figure 3. Due to the visual differences, incorporated in s-AMS of different output representations, our proposed framework is able to clearly distinguish between logits corresponding to classes from the two different datasets, which we can observe from the visible block structure of the computed EA distance matrix and from the representation atlas. DORA is based on the network's ability to perceive self-generated s-AMS and we can observe a clear difference between the patterns of s-AMS for Tiny ImageNet classes, containing high-level natural concepts, and the more data-specific patterns for EMNIST classes, illustrating the network's perception of white-on-black handwritten digits and letters.

4 Evaluation

To demonstrate the usefulness of the proposed distance metric, we conducted a quantitative comparison between the EA distance metric and the semantic baseline, in the scenario, where the baseline for the distance between representations is available. For this purpose, we calculated the EA distances in both a pair-wise and layer-wise manner between the output logits of image classification networks trained on two widely used computer vision datasets, ILSVRC2012 Deng et al. (2009) and CIFAR-100 Krizhevsky (2009).

Baseline semantic distances were obtained by mapping the classification labels to entities in the WordNet taxonomy database Miller (1995), a lexical database that organizes English words into a taxonomy of synonym sets, or synsets. In this taxonomy, each synset represents a group of words that are synonyms or have the same meaning. WordNet organizes these synsets into a hierarchy, with more specific concepts being nested under more general ones. For the ImageNet dataset, class labels were mapped automatically due to the cross-connection with WordNet synsets, while for CIFAR-100 labels were matched manually. The baseline semantic distances between entities from the WordNet database were computed using two distance measures:

- **Shortest-Path distance:** the distance between two classes is determined by the length of the shortest path that connects the two entities in the taxonomy.

  $$d_{SP}(c_i, c_j) = l(c_i, c_j),$$

  where $l(c_i, c_j)$ is the length of the shortest path between classes c_i, c_j.

- **Leacock-Chodorow distance:** a version of the shortest-path distance with additional scaling by the taxonomy depth Leacock and Chodorow (1998):

  $$d_{LC}(c_i, c_j) = \log \frac{l(c_i, c_j) + 1}{2T} - \log \frac{1}{2T}.$$

While it has been reported that taxonomy-based approaches can be suboptimal to taxonomy-free methods Binder et al. (2012), the visual similarity of concepts is strongly coherent with the semantic similarity. In recent years, the relationship between visual and semantic similarities in Computer Vision was studied and a significant linkage has been shown Brust and Denzler (2019). In Deselaers and Ferrari (2011), the authors confirm the assumption that for the ImageNet dataset visual similarity between categories grows with semantic similarity.

To evaluate the alignment between the proposed distance metric and human-defined baseline, we employed the Mantel Test Mentel (1967), which is often employed in ecology and evolutionary biology to measure the correlation between two distance matrices. The test calculates the correlation coefficient ρ, which indicates the strength of the relationship between the two matrices, and the p-value of the test, which describes the statistical significance of the correlation.

4.1 Hyperparameter selection

The quality of distances obtained with the EA metric depends on the selection of hyperparameters. In the following experiment, we sought to understand the influence of two hyperparameters: n, which controls the number of s-AMS samples generated per representation, and m, which controls the number of optimization steps (epochs) for the Feature Visualization method. To conduct this experiment, we utilized the standard ResNet-18 model He et al. (2016) trained on the ImageNet dataset, which is available through the `TorchVision` library Marcel and Rodriguez (2010). The number of samples n ranged from 1 to 100, and the number of optimization epochs m ranged from 1 to 500. The results of our comparison are shown in Figure 4 for both pair-wise and layer-wise settings, illustrating the effect of hyperparameters on Mantel test statistic ρ using the shortest-path semantic baseline for comparison. From these results, we can observe that the number of epochs m has a greater influence on the correlation with ground truth than the number of samples n – the coherence with the ground truth increases as the number of optimization steps increases, and optimal performance is already achieved with only a few s-AMS samples per representation. Additionally, we observe that the layer-wise DORA method, which uses all neurons as descriptors for s-AMS, outperforms the pair-wise method. EA distances obtained from both layer-wise and pair-wise approaches are illustrated in Figure 5, together with semantic distance matrices, obtained from the respective taxonomy Miller (1995).

4.2 Evaluation with ground truth

In this experiment, we quantitatively assess the ability of our proposed method to conserve the semantic distance between representations across different datasets and architectures. To this end, we used eight

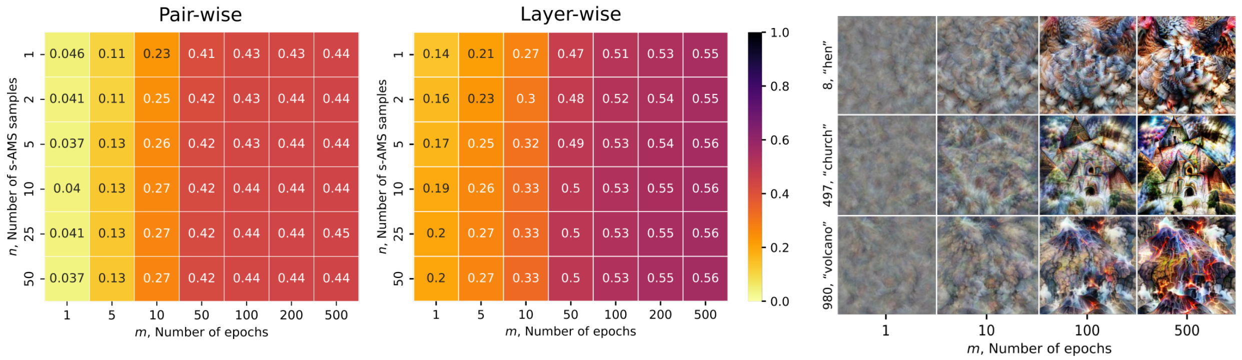

Figure 4: **The influence of hyperparameter selection on the alignment with semantic distance.** The Mantel test results for the comparison of pair-wise and layer-wise EA metrics, computed over the logit layer of ImageNet pre-trained ResNet18 He et al. (2016), with the shortest-path semantic distance baseline are shown on the left, and the impact of the number of optimization steps on s-AMS generation is depicted on the right for 3 ImageNet logit representations obtained the same network. The results (the higher the score, the better) indicate that the number of epochs for s-AMS generation, controlled by the parameter m, has a greater impact than the number of samples per representation n. The layer-wise EA also outperforms the pair-wise metric, implying that incorporating a higher number of descriptors in the s-AMS embedding is beneficial.

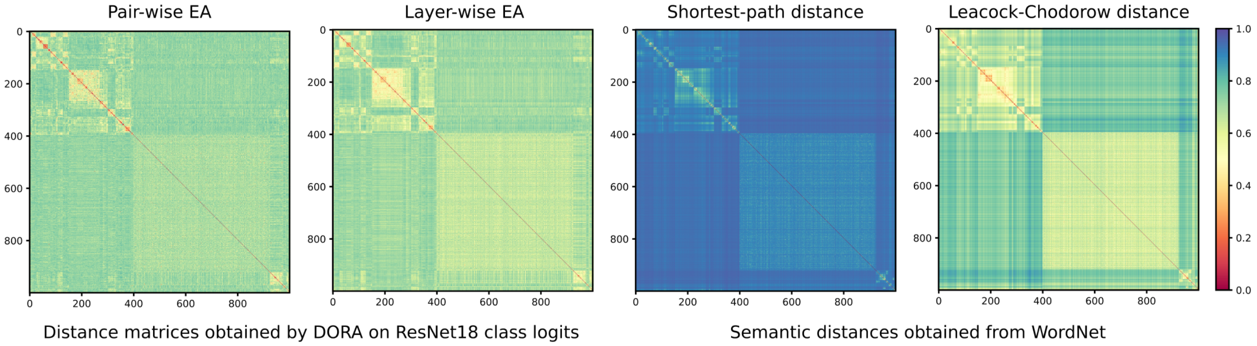

Distance matrices obtained by DORA on ResNet18 class logits

Semantic distances obtained from WordNet

Figure 5: **Similarity between EA distances and taxonomy baseline distances.** The EA distances $(n = 50, m = 500)$ between 1000 logit representations from the output layer of ImageNet-trained ResNet18, both in pair-wise and layer-wise fashion, are illustrated on the left, with semantic baseline distances between labels obtained from the WordNet taxonomy illustrated on the right. We can observe a connection between the baseline semantic distances and the distances obtained via Extreme-Activation metric in a data-agnostic manner by the visual similarity of distance matrices .

different architectures for two datasets, ImageNet and CIFAR100. For ImageNet, we employed ResNet18 He et al. (2016), AlexNet Krizhevsky et al. (2017), ViT Dosovitskiy et al. (2020), BEiT Bao et al. (2021), Inception V3 Szegedy et al. (2016), DenseNet 161 Huang et al. (2017), MobileNet V2 Sandler et al. (2018), ShuffleNet V2 Ma et al. (2018), while for CIFAR-100, we used ResNet 18, ResNet 9, MobileNet V2, ShuffleNet V1, and V2, as well as NASNet Qin and Wang (2019), SqueeeNet Iandola et al. (2016) and VGG 11 Simonyan and Zisserman (2014). We computed EA distances for the output logit layer of all the networks in both layer-wise (l-w) and pair-wise (p-w) scenarios, with $n = 3$ and $m = 500$. The results of the evaluation can be found in Table 1, where the Mantel correlation test statistics ρ is stated for both the layer-wise and pair-wise versions between the computed EA distance and the two semantic distance baselines. From the results, we can observe that the distance obtained by the layer-wise EA metric is more favorable over the pair-wise one due to its stronger linear relationship with both baseline metrics. As a sanity check, an additional experiment was carried out, where EA distances were computed over random noise signals for all networks and both

Table 1: **Correlation between EA distance matrices and semantic distance baselines.** Correlation coefficients ρ (higher is better) obtained from the Mantel test between pair-wise (p-w) and layer-wise (l-w) EA distances and shortest-path (d_{SP}) and Leacock-Chodorow (d_{LC}) semantic distances. All results show statistical significance with $p < 0.001$.

	ImageNet					*CIFAR-100*			
	d_{SP}		d_{LC}			d_{SP}		d_{LC}	
	p-w	*l-w*	*p-w*	*l-w*		*p-w*	*l-w*	*p-w*	*l-w*
ResNet 18	0.44	**0.56**	0.40	**0.53**	*ResNet 9*	0.33	**0.34**	0.3	**0.32**
AlexNet	0.48	**0.51**	0.46	**0.52**	*ShuffleNet V2*	0.47	**0.50**	0.45	**0.50**
ViT	0.50	**0.53**	0.49	**0.55**	*MobileNet V2*	0.42	**0.44**	0.41	**0.44**
BEiT	0.43	**0.50**	0.39	**0.48**	*ResNet 18*	0.33	**0.39**	0.32	**0.39**
Inception V3	0.24	**0.27**	0.20	**0.23**	*ShuffleNet*	0.46	**0.49**	0.45	**0.49**
DenseNet161	0.37	**0.44**	0.32	**0.40**	*VGG 11 BN*	0.26	**0.27**	0.25	**0.26**
MobileNet V2	0.47	**0.59**	0.43	**0.58**	*NasNet*	0.39	**0.41**	0.38	**0.42**
ShuffleNet V2	**0.21**	0.14	**0.17**	0.10	*SqueezeNet*	0.48	**0.51**	0.46	**0.51**

datasets. The results revealed that the test statistics were approximately zero and statistical significance was not demonstrated at a significance level of $\alpha = 0.05$ for all the models.

4.3 Evaluating anomaly-identification capabilities

The ability of EA distances to maintain semantic distances allows the DORA framework to not only detect and display clusters of semantically similar representations via representation atlases but also identify anomalous representations that semantically differ from the majority. While these representations may simply learn unique individual concepts, we demonstrate in further experiments that they might also have learned undesired concepts from spurious correlations in the training data that diverge from the typical (intended) decision-making strategy.

To assess the ability of DORA to detect anomalous representations, we conducted the experiment by inserting random representations in the network layer and evaluating the ability of different Outlier Detection (OD) methods (see e.g. Ruff et al. (2021)) to identify unnatural functions. We employed an ImageNet pre-trained ResNet18 and inserted a set of additional 25 random representations to the average pooling layer of the network, containing 512 learned representations, resulting in a total of 537 representations. These 25 representations were not learned but were constructed as linear combinations of existing representations from various layers within the network. The experiment was conducted in five different scenarios, in which inserted representations were constructed as linear combinations of representations from different layers of the network, namely the “maxpool” (layer preceding the “layer1”), “layer1”, “layer2”, “layer3”, and “layer4”. The weights for the linear combinations were randomly drawn from a standard normal distribution. For each scenario, we estimated the EA distance both pair-wise (p-w) and layer-wise (l-w) and used the resulting distances in five different Outlier Detection methods: the Angle-based Outlier Detector (ABOD) Kriegel et al. (2008), Feature Bagging (FB) Lazarevic and Kumar (2005), Isolation Forest (IF) Liu et al. (2008), Local Outlier Factor (LOF) Breunig et al. (2000) and One-class SVM (OCSVM) Schölkopf et al. (2001). The performance of the Outlier Detection (OD) methods was evaluated using the AUC ROC metric for the classification between existing (learned) representations in the layer, and randomly generated ones. To ensure stability in light of the stochastic nature of some outlier detection methods, the results of the outlier detection were repeated 10 times with different random states. In addition, for each scenario, the linear combinations for the added representations were computed five times. The classification performance for each outlier detection method was then averaged per scenario.

Table 2 presents the results of the described experiment, which demonstrates that all of the Outlier Detection methods performed well in terms of detecting the randomly generated representations across all scenarios. It is worth noting that the pair-wise EA distance (p-w) performed slightly better for the detection of random

Table 2: **Performance of DORA in detecting random representations.** Each cell represents the average AUC ROC of the Outlier Detection methods, for detecting randomly generated representations, based on different layers of the ResNet18 network.

	"maxpool"		"layer1"		"layer2"		"layer3"		"layer4"	
	p-w	*l-w*	*p-w*	*l-w*	*p-w*	*l-w*	*p-w*	*l-w*	*p-w*	*l-w*
ABOD	0.79	**0.98**	0.74	0.93	0.77	0.80	0.81	0.62	1.00	0.58
FB	0.95	0.92	0.95	**0.96**	0.62	**0.89**	0.60	0.59	**1.00**	0.73
IF	0.76	0.83	0.70	0.63	0.58	0.59	0.63	0.57	**1.00**	0.73
LOF	0.66	0.72	0.68	0.69	0.84	0.63	**0.98**	0.78	**1.00**	0.63
OCSVM	0.62	0.84	0.65	0.79	0.78	0.77	0.88	0.78	0.61	0.70

representations. Additionally, the results indicate that different layers of the network have an impact on the detection of random representations, as the Outlier Detection methods performed better when detecting representations generated from higher-level concepts, such as "layer2", "layer3", and "layer4", likely due to the fact that the analysis is performed on the average pooling layer, the last layer of the feature extractor of the network. The high detection rate of randomly initialized representations illustrates the ability of DORA to maintain semantic similarity between learned representations and find semantically anomalous representations.

5 Experiments

As previously demonstrated, the DORA framework facilitates the visualization of a topological map of representations in a designated layer and is able to identify outlier representations. In this section, we aim to investigate the latent representations of widely-used computer vision architectures and demonstrate that the outlier representations found by DORA in real-life scenarios may align with undesirable Clever-Hans concepts and deviate from the intended decision-making approach.

5.1 ImageNet pre-trained networks

Pre-trained networks on ImageNet have become an essential component in the field of Computer Vision. Their capability to recognize a diverse set of objects and scenes makes them particularly useful as a starting point for a wide range of computer vision tasks. They are frequently utilized for fine-tuning to specific tasks or as a feature extractor, where the images are encoded by the networks for further computations Zhuang et al. (2020); Weiss et al. (2016).

In the following we explore the feature extractor representations of three widely-used pre-trained models: ResNet18 He et al. (2016), MobileNetV2 Sandler et al. (2018), and DenseNet121 Huang et al. (2017). Using LOF outlier detection, we found latent layers with representations that appear to be watermark detectors, e.g., detecting Chinese and Latin text patterns. As ImageNet does not have a specific category for watermarks, these representations could be seen as Clever-Hans artifacts and deviate from desired decision-making Lapuschkin et al. (2019); Anders et al. (2022). To verify these representations can detect watermarks, we created two binary classification datasets, for Chinese and Latin watermarks, containing normal images and identical images, with inserted random watermarks, evaluating the sensitivity of individual representations using the AUC ROC classification measure. To ensure the detection of characters and not specific words/phrases (unlike CLIP models Goh et al. (2021)), the probing datasets were generated with random characters (for more details we refer to the Appendix). Our results show that not only the reported outliers but also neighboring representations in EA distance are affected by artifactual behavior. Lastly, we find that this behavior persists during transfer learning, posing a risk for safety-critical fields like medicine.

ImageNet ResNet18

We applied DORA to analyze the Average Pooling layer, which consists of the last 512 high-level representations of the "feature extractor" that are commonly used without further modification during transfer learning.

Following the DORA approach, we calculated EA layer-wise distance with $n = 5$ s-AMS per each representation and with $m = 500$, based on our findings in the section 4.1. After calculating the EA distances, we used the LOF method with a contamination parameter $p = 0.01$ (corresponding to the top 1% of representations) and the number of neighbors was set to 20 (the default value used in the `sklearn` package Pedregosa et al. (2011)).

DORA identified five outlier representations, namely neurons 7, 99, 154, 160, 162, and 393. The outlier neuron 154, displayed a specific, recognizable pattern in s-AMS that could be perceived as the presence of Chinese logograms. By probing the network on a binary classification problem between images watermarked with Chinese logograms vs normal images, Neuron 154 showed a strong detection rate (AUC ROC of 0.94) towards the class with watermarked images, providing significant evidence that this representation is susceptible to the Clever-Hans effect. Further analysis of neighboring representations in EA distance showed that they also exhibit similar behavior. The results of the analysis of the ResNet 18 average pooling layer are shown in Figure 6, illustrating the cluster of Clever-Hans representations found, along with their s-AMS and AUC ROC performance on the binary classification problem. Additional information on the dataset generation and the identified outlier representations can be found in the appendix. Furthermore, the high sensitivity of these representations in terms of their ability to detect artifacts in the data suggests a possible application for using such representations to identify artifacts in training data. Note that in general, the presence of such artifacts could indeed pose serious risks and may lead to a degradation in classifier performance (see Anders et al. (2022)).

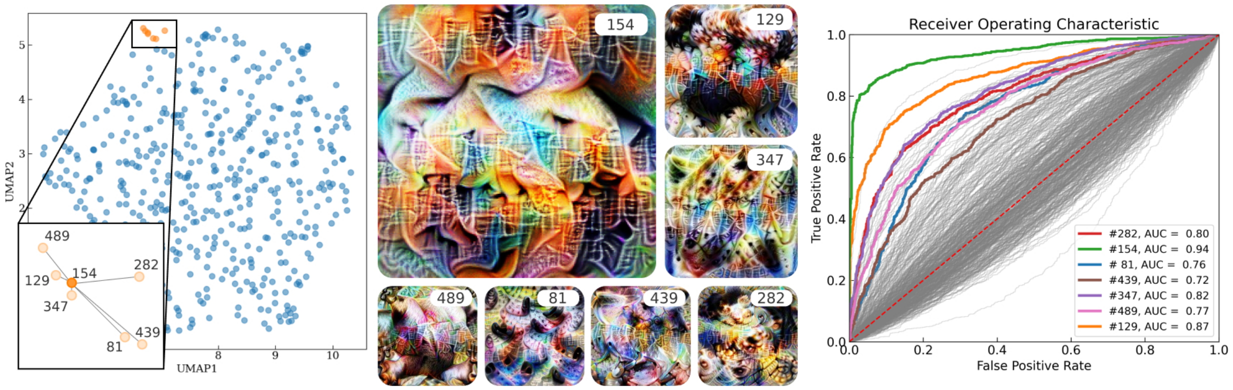

Figure 6: **Cluster of Clever-Hans representations in the ResNet18 feature extractor.** From left to right: representation atlas of the ResNet 18 average pooling layer with the highlighted cluster of Clever-Hans representations (left), s-AMS of the representations in the cluster (middle), and AUC ROC sensitivity scores for the detection of images with Chinese watermarks in the binary classification problem(right), where colored curves correspond to the behavior of representations in the cluster and gray curves for other representations. From the s-AMS of neuron 154, we can observe symbolic patterns resembling Chinese logograms learned by the neuron as well as by its closest neighbor neurons. We can observe that the outlier neuron 154 exhibits the highest AUC value (green curve), followed by its nearest neighbors.

In the further investigation of the model, we inferenced s-AMS signals of representations in the reported CH-cluster and obtained their predictions by the model. Among the selected signals, the model predominantly predicted an affiliation of these signals with the classes “carton”, “swab”, “apron”, “monitor” and “broom”, which is in line with the reported spurious correlation of the “carton” class and Chinese watermarks Li et al. (2022). Upon computing the corresponding s-AMS signals for these logits, we were able to confirm their association with CH-behaviour, as they displayed clear, visible logographic patterns, specific to Chinese character detectors, in their corresponding s-AMS. Corresponding signals and additional information could be found in Appendix.

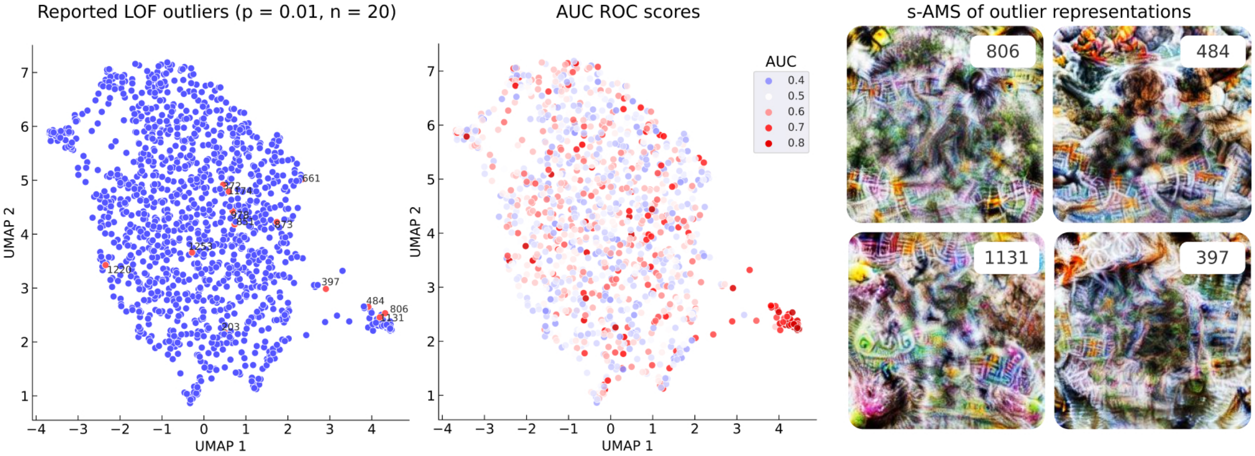

Figure 7: **Cluster of Clever-Hans representations in the MobileNet V2 feature extractor.** The left figure illustrates the outlier representations as identified by the LOF OD method, overlaid on the DORA representation atlas. The middle figure displays the sensitivity of the neural representations to Chinese watermarks, where the highly-sensitive cluster of neurons can be clearly observed in the bottom-right part of the atlas, including 3 reported outlier representations. The right graph illustrates the s-AMS of several of the reported outlier neurons, which exhibit a distinctive logographic pattern typical of Chinese character detectors.

ImageNet MobileNetV2

We used DORA with the same parameters as in the previous experiment ($n = 5$ s-AMS per each representation and $m = 500$ epochs for s-AMS generation) to analyze the "features" layer of MobileNetV2 network Sandler et al. (2018), which consists of 1280 channels with 7×7 activation maps. The analysis was performed on channels by averaging the resulting activation maps of neurons. We calculated the EA distances between representations and applied the LOF method with a contamination parameter of 0.01 which yielded 13 outlier representations. Upon visual inspection of the s-AMS of these representations, we observed distinct patterns specific to Chinese character detectors in neurons 397, 484, 806, and 1131. Figure 7 illustrates the s-AMS of these neurons, as well as the sensitivity of neurons in the Chinese-character detection task. We can observe that the neighbors of these neurons (397, 484, 806, 1131) are sensitive to CH artifacts and form a distinctive cluster visible in the representation atlas.

ImageNet DenseNet 121

We conducted a similar analysis on the last layer of the feature extractor of the ImageNet pre-trained DenseNet121 model, which consists of 1024 channel representations with 7×7 activation maps. We calculated $n = 5$ s-AMS per representation with $m = 150$ optimization steps for quicker experimentation. The LOF outlier detection method with a contamination parameter of $p = 0.01$ identified 10 outlier representations. One of these, neuron 768, was found to be a Chinese character detector (more information can be found in the Appendix). By increasing the contamination parameter to $p = 0.035$ (corresponding to the top 3.5% or 35 representations), we also identified neuron 427, which is susceptible to the detection of Latin text and watermarks. Figure 9 illustrates the representation atlas, highlighting representation 427 along with several neighboring repre-

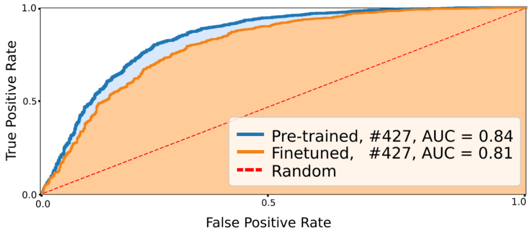

Figure 8: **Persistent Latin text detector**. Neuron 427 in the DenseNet121 network learns to detect Latin text during pre-training and does not unlearn this behavior after fine-tuning on the CheXpert dataset, as shown by the ROC detection curves. The AUC values of the neuron activations on images corrupted with Latin watermarks are high after pre-training and persist after fine-tuning.

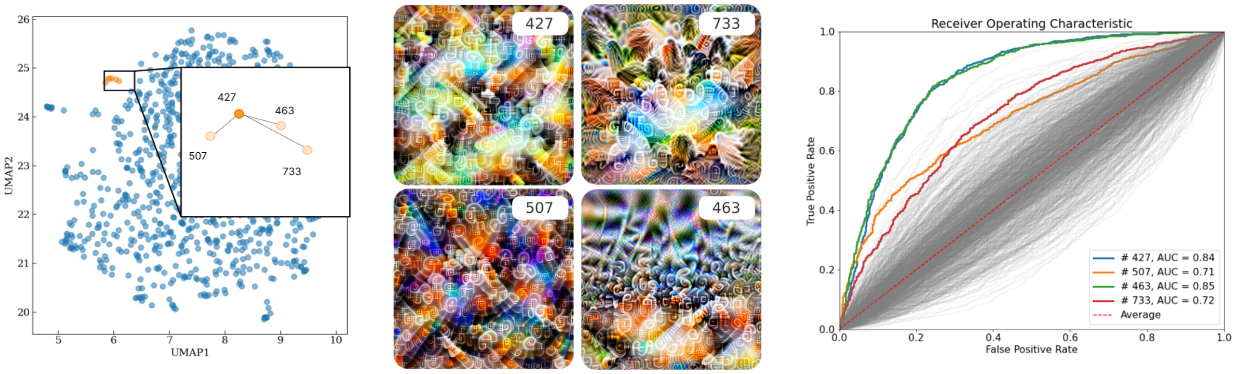

Figure 9: **DenseNet121 — Latin text detector.** Applying DORA to the last layer of the feature extractor of DenseNet121 yields, among others, Neuron 427 as an outlier, which corresponds to the upper left of the 4 feature visualizations. From neuron 427 as well as from its three closest neighbors (shown left), we can observe semantic concepts resembling Latin text characters. The AUC values were computed using the average channel activations on the Latin probing dataset. As shown, the AUCs are high for the representation outliers found by DORA, compared to most of the other representations, which indicates that they indeed learned to detect Latin text patterns.

sentations, namely neurons 733, 507, and 463, which also exhibit a high detection rate for unintended concepts.

Clever Hans representations survive transfer learning

Given the widespread use of pre-trained models in safety-critical areas, it is essential that the artifacts embodied in a pre-trained model are made ineffective or unlearned during the transfer learning task (see also Anders et al. (2022)). To this end, we examined the effect of fine-tuning the pre-trained DenseNet121 model on the CheXpert challenge Irvin et al. (2019), which benchmarks classifiers on a multi-label chest radiograph dataset. Despite the modification of all model parameters during fine-tuning, neurons 427 and 768, which were Latin and Chinese characters detectors in the pre-trained model, retained their original semantic information and remained outliers after applying DORA. We studied neuron 427's ability to detect Latin text and found that it had an AUC value of 0.84 in the pre-trained model and 0.81 in the fine-tuned model, as shown in Figure 8. Similar behavior was observed with neuron 768, indicating that the Clever-Hans effect persisted after fine-tuning.

5.2 CLIP ResNet50

CLIP (Contrastive Language-Image Pre-training) models predict relationships between text and images, trained using contrastive learning objective Dai and Lin (2017); Hjelm et al. (2018) on large datasets and fine-tuned on tasks such as image classification Agarwal et al. (2021) or text-to-image synthesis, where CLIP models also often serve as text encoders (e.g. Stable Diffusion Rombach et al. (2022)).

In this experiment, we explore the representation space of the CLIP ResNet50 model Radford et al. (2021) focusing on the last layer of its image feature extractor ("layer 4"). The training dataset was not publicly disclosed, but it is reported to be much larger than standard computer vision datasets like ImageNet, resulting in greater variability of concepts compared to ImageNet networks. We used DORA on 2048 channel representations from "layer 4", generating $n = 3$ signals per representation with $m = 512$ and using similar settings as (Goh et al., 2021).

Analysis of the outlier representations with contamination parameter $p = 0.0025$ yielded 6 outlier neurons, namely 631, 658, 838, 1666, 1865, and 1896. Representation 1865 – neuron with the highest outlier score – was found to detect the unusual concept of white images/background, as shown by synthetic and natural (collected from `OpenAI Microscope`) AMS in the Figure 10. However, the other outlier representations could not be concluded to be undesirable as they seemed to detect rare but natural concepts. Further details and analysis of the other outlier representations can be found in the Appendix.

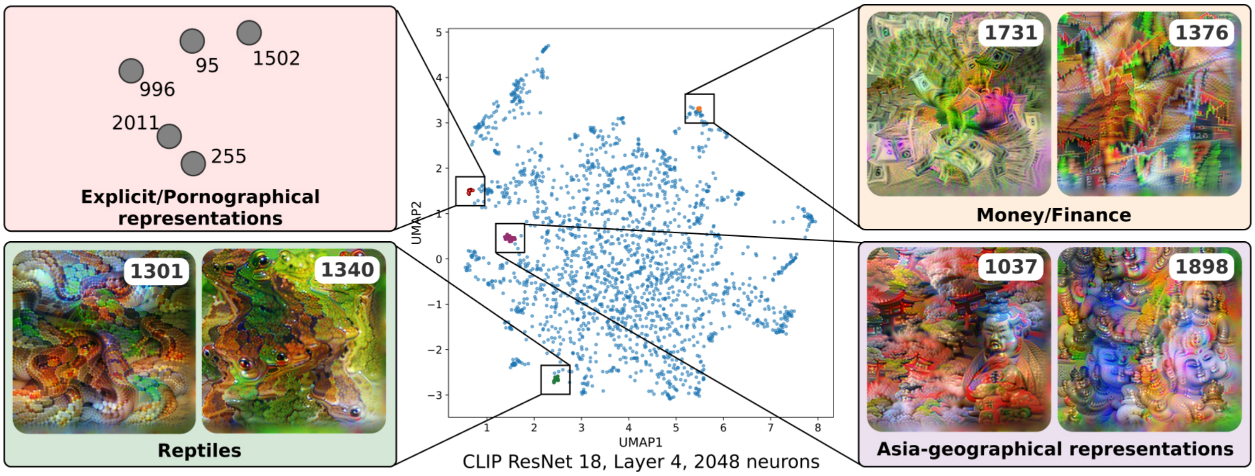

Figure 11: **Representation atlas of CLIP ResNet50 "layer 4".** Representation atlas for CLIP ResNet50 "layer 4", where several clusters of representations are highlighted. Activation-Maximisation signals associated with the Explicit/Pornographic representations were omitted due to the presence of explicit concepts in the signals.

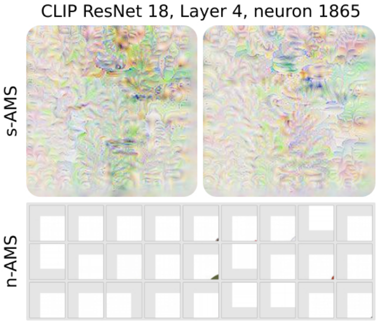

Figure 10: **AMS for reported outlier representation**. LOF identified neuron 1865 as the strongest outlier. Analysis of s-AMS and ImageNet n-AMS indicate that it primarily detects white images/backgrounds, which is atypical compared to other high-level representations in the same layer.

After computing the representation atlas for "layer 4", we manually investigated several distinctive clusters. Figure 11 illustrates the representation atlas alongside several reported clusters of semantically similar representations. With our analysis, we found a cluster of Explicit/Pornographic representations. Furthermore, we were able to confirm the presence of geographical neurons, as reported in (Goh et al., 2021) and we noted that representations from neighboring geographical regions, such as India, China, Korea, and Japan, were located close to one another. Additional information and more detailed visualizations can be found in the Appendix.

6 Discussion and Conclusion

Learned representations in Deep Neural Networks embody the task-relevant (see Braun et al. (2008); Montavon et al. (2011)) the essence of the training data. Since it is not uncommon for datasets to contain artifacts, spurious correlations, or biases, it is more than ever essential to inspect these models using explainable artificial intelligence (XAI) methods to avoid undesirable or even harmful behavior. So far, this has mostly been done by applying local XAI methods, which require access to the data in order to explain the prediction of the model at hand, and, to the best of our knowledge, no method existed to identify representations that have learned unintended or malicious concepts.

The proposed DORA framework is simple and data-independent, allowing the inspection of any trained neural network without access to the training data. It employs the self-explanatory capabilities of Computer Vision networks to estimate distances within the network itself. We found that representations that deviate from desired decision-making strategies typically manifest themselves as outliers in the representation space, which we are able to identify by our proposed method DORA. This can be used to analyze datasets for sensitivity to certain artifact concepts encoded in these outlier representations. We also demonstrated that such outlier representations can persist after transfer learning, highlighting the potential for pre-trained models in safety-critical areas to contain undesired behavior even after fine-tuning on a new dataset.

While we have demonstrated the broad applicability of DORA, there are still some challenges that need to be addressed. The main limitation is the assumption that malicious or CH-behaviour in the representations is not systematic. In other words, DORA may not be able to detect infected representations if this behavior is prevalent across a large number of representations, as it would no longer be perceived as anomalous behavior. Another limitation is the potential semantic multimodality of representations Goh et al. (2021), which DORA attempts to mitigate by computing several s-AMS per representation. However, this may not be sufficient to uncover all of the concepts that a representation is capable of detecting.

In summary, we showed the functionality and usefulness of DORA for finding artifactual aspects in representation space for both controlled and real-world environments. Additionally, the representation atlas, computed by DORA was shown to be a powerful tool for understanding the topological landscape of representations, allowing to visually illustrate the semantic similarities between representations. Note, that although we have introduced DORA as an automatic tool, if necessary, the final decision on the degree of harmfulness of any outlier representations needs to be subject to human scrutiny. In this sense, DORA substantially facilitates human intervention and reduces it to a minimum, however, for safety-critical applications human supervision will still be necessary. In future work, we will apply the proposed solution broadly in the sciences, medicine, and other technical domains, such as NLP, where discovering artifacts and biases in the representations is of great value.

References

GitHub - weiaicunzai/pytorch-cifar100: Practice on CIFAR100— github.com. `https://github.com/weiaicunzai/pytorch-cifar100`, 2020. [Accessed 08-Jan-2023].

S. Agarwal, G. Krueger, J. Clark, A. Radford, J. W. Kim, and M. Brundage. Evaluating CLIP: towards characterization of broader capabilities and downstream implications. *arXiv preprint arXiv:2108.02818*, 2021.

C. J. Anders, L. Weber, D. Neumann, W. Samek, K.-R. Müller, and S. Lapuschkin. Finding and removing clever hans: Using explanation methods to debug and improve deep models. *Information Fusion*, 77:261–295, 2022.

S. Bach, A. Binder, G. on, F. Klauschen, K.-R. Müller, and W. Samek. On pixel-wise explanations for non-linear classifier decisions by layer-wise relevance propagation. *PloS one*, 10(7):e0130140, 2015.

D. Baehrens, T. Schroeter, S. Harmeling, M. Kawanabe, K. Hansen, and K.-R. Müller. How to explain individual classification decisions. *Journal of Machine Learning Research*, 11(Jun):1803–1831, 2010.

H. Bao, L. Dong, and F. Wei. BEIT: BERT pre-training of image transformers. *arXiv preprint arXiv:2106.08254*, 2021.

D. Bau, B. Zhou, A. Khosla, A. Oliva, and A. Torralba. Network dissection: Quantifying interpretability of deep visual representations. In *Proceedings of the IEEE Conference on Computer Vision and Pattern Recognition*, pages 6541–6549, 2017.

D. Bau, J.-Y. Zhu, H. Strobelt, B. Zhou, J. B. Tenenbaum, W. T. Freeman, and A. Torralba. GAN dissection: Visualizing and understanding generative adversarial networks. *arXiv preprint arXiv:1811.10597*, 2018.

Y. Bengio, A. Courville, and P. Vincent. Representation learning: A review and new perspectives. *IEEE transactions on pattern analysis and machine intelligence*, 35(8):1798–1828, 2013.

F. Bießmann, F. C. Meinecke, A. Gretton, A. Rauch, G. Rainer, N. K. Logothetis, and K.-R. Müller. Temporal kernel CCA and its application in multimodal neuronal data analysis. *Machine Learning*, 79(1):5–27, 2010.

A. Binder, K.-R. Müller, and M. Kawanabe. On taxonomies for multi-class image categorization. *International Journal of Computer Vision*, 99(3):281–301, 2012.

S. Bird, E. Klein, and E. Loper. *Natural language processing with Python: analyzing text with the natural language toolkit*. O'Reilly Media, Inc., 2009.

E. Bisong and E. Bisong. Google colaboratory. *Building machine learning and deep learning models on google cloud platform: a comprehensive guide for beginners*, pages 59–64, 2019.

R. Bommasani, D. A. Hudson, E. Adeli, R. Altman, S. Arora, S. von Arx, M. S. Bernstein, J. Bohg, A. Bosselut, E. Brunskill, et al. On the opportunities and risks of foundation models. *arXiv preprint arXiv:2108.07258*, 2021.

J. Borowski, R. S. Zimmermann, J. Schepers, R. Geirhos, T. S. Wallis, M. Bethge, and W. Brendel. Natural images are more informative for interpreting cnn activations than state-of-the-art synthetic feature visualizations. In *NeurIPS 2020 Workshop SVRHM*, 2020.

M. L. Braun, J. M. Buhmann, and K.-R. Müller. On relevant dimensions in kernel feature spaces. *The Journal of Machine Learning Research*, 9:1875–1908, 2008.

M. M. Breunig, H.-P. Kriegel, R. T. Ng, and J. Sander. LOF: identifying density-based local outliers. In *Proceedings of the 2000 ACM SIGMOD International Conference on Management of data*, pages 93–104, 2000.

K. E. Brown and D. A. Talbert. Using explainable AI to measure feature contribution to uncertainty. In *The International FLAIRS Conference Proceedings*, volume 35, 2022.

T. Brown, B. Mann, N. Ryder, M. Subbiah, J. D. Kaplan, P. Dhariwal, A. Neelakantan, P. Shyam, G. Sastry, A. Askell, et al. Language models are few-shot learners. *Advances in Neural Information Processing Systems*, 33:1877–1901, 2020.

C.-A. Brust and J. Denzler. Not just a matter of semantics: The relationship between visual and semantic similarity. In *German Conference on Pattern Recognition*, pages 414–427. Springer, 2019.

V. Buhrmester, D. Münch, and M. Arens. Analysis of explainers of black box Deep Neural Networks for Computer Vision: A survey. *arXiv preprint arXiv:1911.12116*, 2019.

K. Bykov, M. M.-C. Höhne, A. Creosteanu, K.-R. Müller, F. Klauschen, S. Nakajima, and M. Kloft. Explaining Bayesian Neural Networks. *arXiv preprint arXiv:2108.10346*, 2021.

K. Bykov, A. Hedström, S. Nakajima, and M. M.-C. Höhne. NoiseGrad—enhancing explanations by introducing stochasticity to model weights. In *Proceedings of the AAAI Conference on Artificial Intelligence*, volume 36, pages 6132–6140, 2022.

S. Carter, Z. Armstrong, L. Schubert, I. Johnson, and C. Olah. Exploring Neural Networks with activation atlases. *Distill.*, 2019.

C. Chen, O. Li, C. Tao, A. J. Barnett, J. Su, and C. Rudin. This looks like that: deep learning for interpretable image recognition. *arXiv preprint arXiv:1806.10574*, 2018.

G. Cohen, S. Afshar, J. Tapson, and A. Van Schaik. Emnist: Extending mnist to handwritten letters. In *2017 International joint Conference on neural networks (IJCNN)*, pages 2921–2926. IEEE, 2017.

J. Da. A corpus-based study of character and bigram frequencies in chinese e-texts and its implications for chinese language instruction. In *Proceedings of the fourth International Conference on new technologies in teaching and learning Chinese*, pages 501–511. Citeseer, 2004.

B. Dai and D. Lin. Contrastive learning for image captioning. *Advances in Neural Information Processing Systems*, 30, 2017.

J. Deng, W. Dong, R. Socher, L.-J. Li, K. Li, and L. Fei-Fei. Imagenet: A large-scale hierarchical image database. In *2009 IEEE Conference on Computer Vision and Pattern Recognition*, pages 248–255. IEEE, 2009.

L. Deng. The MNIST database of handwritten digit images for machine learning research. *IEEE Signal Processing Magazine*, 29(6):141–142, 2012.

T. Deselaers and V. Ferrari. Visual and semantic similarity in imagenet. In *CVPR 2011*, pages 1777–1784. IEEE, 2011.

A. Dosovitskiy, L. Beyer, A. Kolesnikov, D. Weissenborn, X. Zhai, T. Unterthiner, M. Dehghani, M. Minderer, G. Heigold, S. Gelly, et al. An image is worth 16x16 words: Transformers for image recognition at scale. *arXiv preprint arXiv:2010.11929*, 2020.

D. Erhan, Y. Bengio, A. Courville, and P. Vincent. Visualizing higher-layer features of a deep network. *University of Montreal*, 1341(3):1, 2009.

I. Fogel and D. Sagi. Gabor filters as texture discriminator. *Biological cybernetics*, 61(2):103–113, 1989.

K. Gade, S. C. Geyik, K. Kenthapadi, V. Mithal, and A. Taly. Explainable AI in industry. In *Proceedings of the 25th ACM SIGKDD International Conference on knowledge discovery & data mining*, pages 3203–3204, 2019.

S. Gautam, M. M.-C. Höhne, S. Hansen, R. Jenssen, and M. Kampffmeyer. This looks more like that: Enhancing self-explaining models by prototypical relevance propagation. *arXiv preprint arXiv:2108.12204*, 2021.

S. Gautam, M. M.-C. Höhne, S. Hansen, R. Jenssen, and M. Kampffmeyer. Demonstrating the risk of imbalanced datasets in chest x-ray image-based diagnostics by prototypical relevance propagation. In *2022 IEEE 19th International Symposium on Biomedical Imaging (ISBI)*, pages 1–5, 2022. doi: 10.1109/ISBI52829.2022.9761651.

R. Geirhos, P. Rubisch, C. Michaelis, M. Bethge, F. A. Wichmann, and W. Brendel. ImageNet-trained CNNs are biased towards texture; increasing shape bias improves accuracy and robustness. *arXiv preprint arXiv:1811.12231*, 2018.

R. Geirhos, J.-H. Jacobsen, C. Michaelis, R. Zemel, W. Brendel, M. Bethge, and F. A. Wichmann. Shortcut learning in deep neural networks. *Nature Machine Intelligence*, 2(11):665–673, 2020.

G. Goh, N. Cammarata, C. Voss, S. Carter, M. Petrov, L. Schubert, A. Radford, and C. Olah. Multimodal neurons in artificial neural networks. *Distill*, 6(3):e30, 2021.

D. Grinwald, K. Bykov, S. Nakajima, and M. M.-C. Höhne. Visualizing the diversity of representations learned by bayesian neural networks. *arXiv preprint arXiv:2201.10859*, 2022.

T. Gu, B. Dolan-Gavitt, and S. Garg. Badnets: Identifying vulnerabilities in the machine learning model supply chain. *arXiv preprint arXiv:1708.06733*, 2017.

R. Guidotti. Evaluating local explanation methods on ground truth. *Artificial Intelligence*, 291:103428, 2021.

R. Guidotti, A. Monreale, S. Ruggieri, F. Turini, F. Giannotti, and D. Pedreschi. A survey of methods for explaining black box models. *ACM computing surveys (CSUR)*, 51(5):1–42, 2018.

I. Guyon and A. Elisseeff. An introduction to variable and feature selection. *Journal of Machine Learning Research*, 3 (Mar):1157–1182, 2003.

D. Hardoon, S. Szedmak, and J. Shawe-Taylor. Canonical Correlation Analysis: An overview with application to learning methods. *Neural computation*, 16:2639–64, 01 2005. doi: 10.1162/0899766042321814.

K. He, X. Zhang, S. Ren, and J. Sun. Deep residual learning for image recognition. In *Proceedings of the IEEE Conference on Computer Vision and Pattern Recognition*, pages 770–778, 2016.

A. Hedström, L. Weber, D. Bareeva, F. Motzkus, W. Samek, S. Lapuschkin, and M. M.-C. Höhne. Quantus: an explainable AI toolkit for responsible evaluation of neural network explanations. *arXiv preprint arXiv:2202.06861*, 2022.

E. Hernandez, S. Schwettmann, D. Bau, T. Bagashvili, A. Torralba, and J. Andreas. Natural language descriptions of deep visual features. In *International Conference on Learning Representations*, 2021.

R. D. Hjelm, A. Fedorov, S. Lavoie-Marchildon, K. Grewal, P. Bachman, A. Trischler, and Y. Bengio. Learning deep representations by mutual information estimation and maximization. *arXiv preprint arXiv:1808.06670*, 2018.

G. Huang, Z. Liu, L. Van Der Maaten, and K. Q. Weinberger. Densely Connected Convolutional Networks. In *Proceedings of the IEEE Conference on Computer Vision and Pattern Recognition*, pages 4700–4708, 2017.

F. N. Iandola, S. Han, M. W. Moskewicz, K. Ashraf, W. J. Dally, and K. Keutzer. Squeezenet: Alexnet-level accuracy with 50x fewer parameters and< 0.5 mb model size. *arXiv preprint arXiv:1602.07360*, 2016.

J. Irvin, P. Rajpurkar, M. Ko, Y. Yu, S. Ciurea-Ilcus, C. Chute, H. Marklund, B. Haghgoo, R. Ball, K. Shpanskaya, J. Seekins, D. Mong, S. Halabi, J. Sandberg, R. Jones, D. Larson, C. Langlotz, B. Patel, M. Lungren, and A. Ng. Chexpert: A large chest radiograph dataset with uncertainty labels and expert comparison. *Proceedings of the AAAI Conference on Artificial Intelligence*, 33:590–597, 07 2019.

P. Izmailov, P. Kirichenko, N. Gruver, and A. G. Wilson. On feature learning in the presence of spurious correlations. *arXiv preprint arXiv:2210.11369*, 2022.

P. Jackson. Introduction to expert systems. URL `https://www.osti.gov/biblio/5675197`. [Accessed 16-Feb-2023].

A. Jaiswal, A. R. Babu, M. Z. Zadeh, D. Banerjee, and F. Makedon. A survey on contrastive self-supervised learning. *Technologies*, 9(1):2, 2020.

H. Jiang and O. Nachum. Identifying and correcting label bias in machine learning. In S. Chiappa and R. Calandra, editors, *Proceedings of the Twenty Third International Conference on Artificial Intelligence and Statistics*, volume 108 of *Proceedings of Machine Learning Research*, pages 702–712. PMLR, 26–28 Aug 2020. URL `https://proceedings.mlr.press/v108/jiang20a.html`.

S. Kornblith, M. Norouzi, H. Lee, and G. Hinton. Similarity of neural network representations revisited. In *International Conference on Machine Learning*, pages 3519–3529. PMLR, 2019.

H.-P. Kriegel, M. Schubert, and A. Zimek. Angle-based outlier detection in high-dimensional data. In *Proceedings of the 14th ACM SIGKDD International Conference on Knowledge discovery and data mining*, pages 444–452, 2008.

A. Krizhevsky. Learning multiple layers of features from tiny images. pages 32–33, 2009. URL `https://www.cs.toronto.edu/~kriz/learning-features-2009-TR.pdf`.

A. Krizhevsky, I. Sutskever, and G. E. Hinton. Imagenet classification with deep convolutional neural networks. *Communications of the ACM*, 60(6):84–90, 2017.

A. Laakso. Content and cluster analysis: Assessing representational similarity in neural systems. *Philosophical Psychology*, 13, 05 2000. doi: 10.1080/09515080050002726.

S. Lapuschkin, A. Binder, G. Montavon, K.-R. Muller, and W. Samek. Analyzing classifiers: Fisher vectors and deep neural networks. In *Proceedings of the IEEE Conference on Computer Vision and Pattern Recognition*, pages 2912–2920, 2016.

S. Lapuschkin, S. Wäldchen, A. Binder, G. Montavon, W. Samek, and K.-R. Müller. Unmasking clever hans predictors and assessing what machines really learn. *Nature communications*, 10:1096, 2019.

A. Lazarevic and V. Kumar. Feature bagging for outlier detection. In *Proceedings of the eleventh ACM SIGKDD International Conference on Knowledge discovery in data mining*, pages 157–166, 2005.

Y. Le and X. Yang. Tiny imagenet visual recognition challenge. *Stanford CS 231N*, 7(7):3, 2015.

C. Leacock and M. Chodorow. Combining local context and wordnet similarity for word sense identification. *WordNet: An electronic lexical database*, 49(2):265–283, 1998.

Y. LeCun and I. Misra. Self-supervised learning: The dark matter of intelligence, 2021. URL `https://ai.facebook.com/blog/self-supervised-learning-the-dark-matter-of-intelligence/`. [Accessed 08-Jan-2023].

Y. Li, J. Yosinski, J. Clune, H. Lipson, and J. Hopcroft. Convergent learning: Do different neural networks learn the same representations? *arXiv preprint arXiv:1511.07543*, 2015.

Z. Li, I. Evtimov, A. Gordo, C. Hazirbas, T. Hassner, C. C. Ferrer, C. Xu, and M. Ibrahim. A whac-a-mole dilemma: Shortcuts come in multiples where mitigating one amplifies others, 2022.

F. T. Liu, K. M. Ting, and Z.-H. Zhou. Isolation Forest. In *2008 8-th IEEE International Conference on Data Mining*, pages 413–422. IEEE, 2008.

N. Ma, X. Zhang, H.-T. Zheng, and J. Sun. Shufflenet v2: Practical guidelines for efficient cnn architecture design. In *Proceedings of the European Conference on Computer Vision (ECCV)*, pages 116–131, 2018.

S. Marcel and Y. Rodriguez. Torchvision the machine-vision package of torch. In *Proceedings of the 18th ACM International Conference on Multimedia*, pages 1485–1488, 2010.

D. Marr and H. K. Nishihara. Representation and recognition of the spatial organization of three-dimensional shapes. *Proceedings of the Royal Society of London. Series B. Biological Sciences*, 200(1140):269–294, 1978.

L. McInnes, J. Healy, N. Saul, and L. Grossberger. Umap: Uniform manifold approximation and projection. *Journal of Open Source Software*, 3:861, 09 2018. doi: 10.21105/joss.00861.

N. Mentel. The detection of disease clustering and a generalized regression approach. *Cancer Res.*, 27:175–178, 1967.

G. A. Miller. Wordnet: a lexical database for english. *Communications of the ACM*, 38(11):39–41, 1995.

G. Montavon, M. L. Braun, and K.-R. Müller. Kernel analysis of deep networks. *Journal of Machine Learning Research*, 12(78):2563–2581, 2011.

G. Montavon, W. Samek, and K.-R. Müller. Methods for interpreting and understanding deep neural networks. *Digital Signal Processing*, 73:1–15, 2018.

A. Morcos, M. Raghu, and S. Bengio. Insights on representational similarity in neural networks with canonical correlation. *Advances in Neural Information Processing Systems*, 31, 2018.

J. Mu and J. Andreas. Compositional explanations of neurons. *Advances in Neural Information Processing Systems*, 33:17153–17163, 2020.

T. Nguyen, M. Raghu, and S. Kornblith. Do wide and deep networks learn the same things? Uncovering how neural network representations vary with width and depth. *arXiv preprint arXiv:2010.15327*, 2020.

T. Nguyen, M. Raghu, and S. Kornblith. On the origins of the block structure phenomenon in neural network representations. *arXiv preprint arXiv:2202.07184*, 2022.

C. Olah, A. Mordvintsev, and L. Schubert. Feature visualization. *Distill*, 2(11):e7, 2017.

D. Omeiza, S. Speakman, C. Cintas, and K. Weldermariam. Smooth Grad-Cam++: An enhanced inference level visualization technique for deep convolutional neural network models. *arXiv preprint arXiv:1908.01224*, 2019.

F. Pedregosa, G. Varoquaux, A. Gramfort, V. Michel, B. Thirion, O. Grisel, M. Blondel, P. Prettenhofer, R. Weiss, V. Dubourg, et al. Scikit-learn: Machine learning in python. *Journal of Machine Learning Research*, 12(Oct): 2825–2830, 2011.

X. Qin and Z. Wang. Nasnet: A neuron attention stage-by-stage net for single image deraining. *arXiv preprint arXiv:1912.03151*, 2019.

A. Radford, J. W. Kim, C. Hallacy, A. Ramesh, G. Goh, S. Agarwal, G. Sastry, A. Askell, P. Mishkin, J. Clark, et al. Learning transferable visual models from natural language supervision. In *International Conference on Machine Learning*, pages 8748–8763. PMLR, 2021.

M. Raghu, J. Gilmer, J. Yosinski, and J. Sohl-Dickstein. SVCCA: Singular Vector Canonical Correlation Analysis for deep understanding and improvement. *arXiv preprint arXiv:1706.05806*, 2017.

M. Raghu, T. Unterthiner, S. Kornblith, C. Zhang, and A. Dosovitskiy. Do vision transformers see like convolutional neural networks? *Advances in Neural Information Processing Systems*, 34:12116–12128, 2021.

J. Ramsay, J. Berge, and G. Styan. Matrix correlation. *Psychometrika*, 49:403–423, 09 1984. doi: 10.1007/BF02306029.

R. Rombach, A. Blattmann, D. Lorenz, P. Esser, and B. Ommer. High-resolution image synthesis with latent diffusion models. In *Proceedings of the IEEE/CVF Conference on Computer Vision and Pattern Recognition (CVPR)*, pages 10684–10695, June 2022.

C. Rudin. Stop explaining black box machine learning models for high stakes decisions and use interpretable models instead. *Nature machine intelligence*, 1(5):206–215, 2019.

L. Ruff, J. R. Kauffmann, R. A. Vandermeulen, G. Montavon, W. Samek, M. Kloft, T. G. Dietterich, and K.-R. Müller. A unifying review of deep and shallow anomaly detection. *Proceedings of the IEEE*, 109(5):756–795, 2021.

W. Samek, A. Binder, G. on, S. Lapuschkin, and K.-R. Müller. Evaluating the visualization of what a deep neural network has learned. *IEEE transactions on Neural Networks and Learning Systems*, 28(11):2660–2673, 2016.

W. Samek, G. Montavon, A. Vedaldi, L. K. Hansen, and K.-R. Müller. *Explainable AI: interpreting, explaining and visualizing deep learning*, volume 11700. Springer Nature, 2019.

W. Samek, G. Montavon, S. Lapuschkin, C. J. Anders, and K.-R. Müller. Explaining deep neural networks and beyond: A review of methods and applications. *Proceedings of the IEEE*, 109(3):247–278, 2021.

M. Sandler, A. Howard, M. Zhu, A. Zhmoginov, and L.-C. Chen. Mobilenetv2: Inverted residuals and linear bottlenecks. In *Proceedings of the IEEE Conference on Computer Vision and Pattern Recognition*, pages 4510–4520, 2018.

B. Schölkopf, J. C. Platt, J. Shawe-Taylor, A. J. Smola, and R. C. Williamson. Estimating the support of a high-dimensional distribution. *Neural computation*, 13(7):1443–1471, 2001.

P. Schramowski, W. Stammer, S. Teso, A. Brugger, F. Herbert, X. Shao, H.-G. Luigs, A.-K. Mahlein, and K. Kersting. Making deep neural networks right for the right scientific reasons by interacting with their explanations. *Nature Machine Intelligence*, 2(8):476–486, 2020.

R. R. Selvaraju, M. Cogswell, A. Das, R. Vedantam, D. Parikh, and D. Batra. Grad-cam: Visual explanations from deep networks via gradient-based localization. *International Journal of Computer Vision*, 128(2):336–359, 10 2019. ISSN 1573-1405. doi: 10.1007/s11263-019-01228-7.

K. Simonyan and A. Zisserman. Very deep convolutional networks for large-scale image recognition. *arXiv preprint arXiv:1409.1556*, 2014.

D. Smilkov, N. Thorat, B. Kim, F. Viégas, and M. Wattenberg. Smoothgrad: removing noise by adding noise. *arXiv preprint arXiv:1706.03825*, 2017.

M. Sundararajan, A. Taly, and Q. Yan. Axiomatic attribution for deep networks. In *International Conference on Machine Learning*, pages 3319–3328. PMLR, 2017.

C. Szegedy, W. Zaremba, I. Sutskever, J. Bruna, D. Erhan, I. Goodfellow, and R. Fergus. Intriguing properties of neural networks. *arXiv preprint arXiv:1312.6199*, 2013.

C. Szegedy, V. Vanhoucke, S. Ioffe, J. Shlens, and Z. Wojna. Rethinking the inception architecture for computer vision. In *Proceedings of the IEEE Conference on Computer Vision and Pattern Recognition*, pages 2818–2826, 2016.

B. Thomee, D. A. Shamma, G. Friedland, B. Elizalde, K. Ni, D. Poland, D. Borth, and L.-J. Li. Yfcc100m: The new data in multimedia research. *Communications of the ACM*, 59(2):64–73, 2016.

E. Tjoa and C. Guan. A survey on Explainable Artificial Intelligence (XAI): Toward medical XAI. *IEEE transactions on Neural Networks and Learning Systems*, 32(11):4793–4813, 2020.

B. Tran, J. Li, and A. Madry. Spectral signatures in backdoor attacks. *Advances in Neural Information Processing Systems*, 31, 2018.

M. M.-C. Vidovic, N. Görnitz, K.-R. Müller, G. Rätsch, and M. Kloft. Opening the black box: Revealing interpretable sequence motifs in kernel-based learning algorithms. In *Joint European Conference on Machine Learning and Knowledge Discovery in Databases*, pages 137–153. Springer, 2015.

M. M.-C. Vidovic, N. Görnitz, K.-R. Müller, and M. Kloft. Feature importance measure for non-linear learning algorithms. *arXiv preprint arXiv:1611.07567*, 2016.

D. Wallis and I. Buvat. Clever hans effect found in a widely used brain tumour mri dataset. *Medical Image Analysis*, 77:102368, 2022.

Y. Wang. CIFAR-100 Resnet PyTorch 75.17% Accuracy — kaggle.com. `https://www.kaggle.com/code/yiweiwangau/cifar-100-resnet-pytorch-75-17-accuracy`, 2021. [Accessed 08-Jan-2023].

K. Weiss, T. M. Khoshgoftaar, and D. Wang. A survey of transfer learning. *Journal of Big data*, 3(1):1–40, 2016.

R. Wightman. Pytorch image models. `https://github.com/rwightman/pytorch-image-models`, 2019.

K. Xiao, L. Engstrom, A. Ilyas, and A. Madry. Noise or signal: The role of image backgrounds in object recognition. *arXiv preprint arXiv:2006.09994*, 2020.

F. Xu, H. Uszkoreit, Y. Du, W. Fan, D. Zhao, and J. Zhu. Explainable AI: A brief survey on history, research areas, approaches and challenges. In *CCF International Conference on natural language processing and Chinese computing*, pages 563–574. Springer, 2019.

Z. Yuan, Y. Yan, M. Sonka, and T. Yang. Large-scale Robust Deep AUC Maximization: A new surrogate loss and empirical studies on medical image classification. pages 3020–3029, 10 2021. doi: 10.1109/ICCV48922.2021.00303.

J. R. Zech, M. A. Badgeley, M. Liu, A. B. Costa, J. J. Titano, and E. K. Oermann. Variable generalization performance of a deep learning model to detect pneumonia in chest radiographs: a cross-sectional study. *PLoS medicine*, 15(11): e1002683, 2018.

M. D. Zeiler and R. Fergus. Visualizing and understanding convolutional networks. In *European Conference on Computer Vision*, pages 818–833. Springer, 2014.

F. Zhuang, Z. Qi, K. Duan, D. Xi, Y. Zhu, H. Zhu, H. Xiong, and Q. He. A comprehensive survey on transfer learning. *Proceedings of the IEEE*, 109(1):43–76, 2020.

A Appendix

A.1 Toy experiment

To illustrate the ability of DORA to detect clusters of semantically similar representations, we trained a model on the combination of 2 datasets: TinyImageNet and EMNIST.

- Tiny-ImageNet Le and Yang (2015) is a small version of the ImageNet dataset, consisting of a subset of images from the ImageNet dataset Deng et al. (2009) and is often used as a more computationally efficient alternative for testing and developing new image classification algorithms. The Tiny-ImageNet dataset contains 200 classes, with 500 images in each class, for a total of 100,000 images. The images are downscaled to 64 x 64 pixels in size and are labeled with one of the 200 class labels.

- EMNIST Cohen et al. (2017) is a dataset of handwritten characters and digits that is widely used in machine learning and computer vision research. The EMNIST dataset was developed as an extension of the original MNIST Deng (2012) dataset, which only contained images of digits, and has proven to be a valuable resource for researchers working in the fields of pattern recognition and machine learning. For this particular application, we employed 47 different classes from the "balanced" split of the dataset, obtained from `torchvision` library Marcel and Rodriguez (2010). For each of the classes, images were resized to 64 x 64 pixels with 3 color channels to share the same dimensions with TinyImageNet, and the number of images per class was set to 200.

The ResNet18 model was utilized for training, initialized with ImageNet pre-trained weights, and the output layers were modified to accommodate the altered input size and the number of classes. The dataset, comprising 109400 images, was divided into training (103930 images), testing (2735 images), and validation (2735 images) sets. The network was trained for 50 epochs using the Adam optimizer with a learning rate of 0.0001 and a batch size of 256, resulting in a model that achieved an accuracy of 0.552 on the validation set.

A.2 Evaluation

In the evaluation, two datasets were used: ILSVRC2012 (ImageNet 2012) Deng et al. (2009) and CIFAR-100 Krizhevsky (2009). For ImageNet, we employed eight different pre-trained models: ResNet18 He et al. (2016), AlexNet Krizhevsky et al. (2017), Inception V3 Szegedy et al. (2016), DenseNet 161 Huang et al. (2017), MobileNet V2 Sandler et al. (2018), ShuffleNet V2 Ma et al. (2018), obtained from the `torchvision-models` package Marcel and Rodriguez (2010), as well as ViT Dosovitskiy et al. (2020) and BEiT Krizhevsky et al. (2017), obtained from the `pytorch-vision-models` library Wightman (2019). For the CIFAR-100 dataset, we trained seven networks: ResNet 18, MobileNet V2, ShuffleNet V1, and V2, NASNet Qin and Wang (2019), SqueeeNet Iandola et al. (2016), and VGG 11 Simonyan and Zisserman (2014), using the `Pytorch-cifar100` GitHub repository git (2020), while the ResNet9 network was trained using a publicly available Kaggle notebook Wang (2021).

The semantic baseline distances between concepts for both datasets were obtained using the `NLTK` package Bird et al. (2009). There is a cross-connection between class labels and WordNet entities for ILSVRC2012, as the classes are inherently connected with WordNet synsets. For CIFAR-100, we manually connected the labels to synsets by matching class label names with WordNet synset names. For 98 classes, WordNet synsets were found. For the remaining two classes, "aquarium fish" and "maple tree", WordNet synsets for "fish" and "maple" were used, respectively, due to the absence of a direct name match.

A.2.1 Hyperparameter selection

In this section, we provide more detailed results for the hyperparameter selection process described in Section 4.1. Figure 17 show the detailed results of the Mantel test for each of the selection of the hyperparameters n and m. These results provide further insight into the effect of different hyperparameter values on the performance of the DORA method.

A.2.2 Evaluating anomaly-identification capabilities

In this experiment, we utilized ResNet18 He et al. (2016). Specifically, we worked with representations that were obtained after the average pooling layer, which contained 512 high-level representations outputting scalar values. During the course of the experiment, we introduced 25 new representations to the same layer. These new representations encoded completely randomized concepts and were generated by constructing each of them in the form of a linear combination with random weights from the existing representations in other layers of the same model. We generated random representations from the following convolution layers by averaging representations across channels to obtain scalar functions:

- *"maxpool"* - a layer of the network preceding the "layer1" layer, containing 64 channels,
- *"layer1"*, containing 64 channel representations,
- *"layer2"*, containing 128 channel representations,
- *"layer3"*, containing 256 channel representations,
- *"layer4"*, containing 512 channel representations, denoting the same representations that are in the average pooling layer.

We generated five instances of random representations for each of the listed five scenarios. We accomplished this by sampling different linear combinations from the standard normal distribution, resulting in five different sets of functions for each scenario. For each of the scenarios, we ran Outlier Detection methods five times for each of the instances to ensure the stability of the OD methods' performance, given the indeterminacy of the employed methods. Each of the mentioned methods was employed with the default hyperparameters from the `sklearn` package Pedregosa et al. (2011). In the final result table, illustrated in Table 2 in the main paper, for each of the five scenarios, the final AUC ROC values were averaged per OD initialization and per instance (for a total of 25 results).

A.3 Experiments

A.3.1 Probing dataset

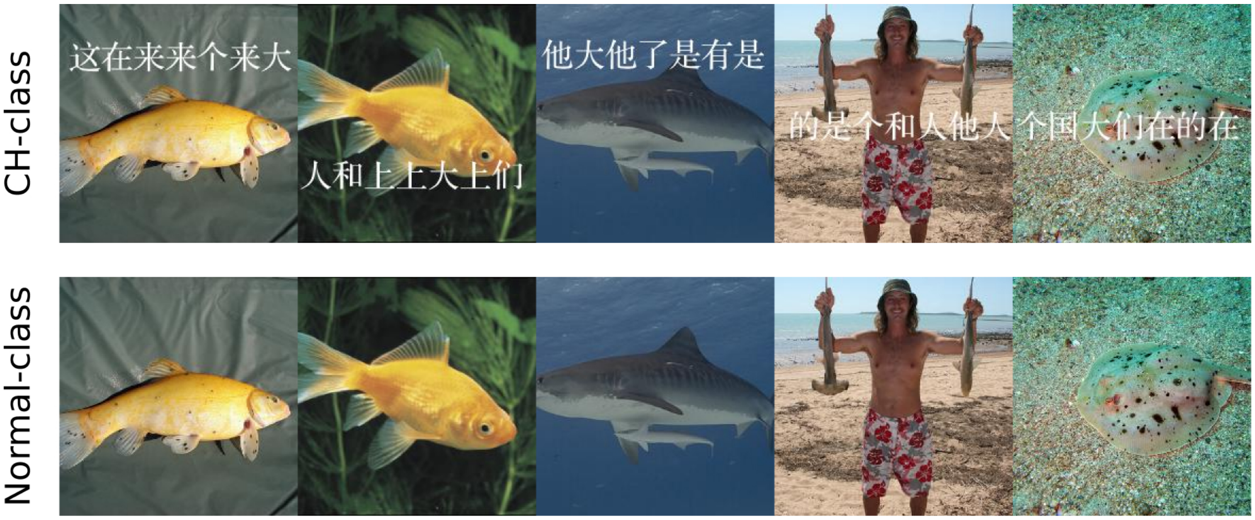

Figure 12: **Illustration of the Probing Dataset.** The figure depicts images from the probing dataset utilized to evaluate the representation's capacity to distinguish between watermarked (CH) and non-watermarked (normal) images. The watermarked class images are identical to the normal class images, except for the addition of a random test string at a random location on the image.

To assess the ability of the identified representations to detect undesirable concepts, we created two probing datasets for the binary classification of Chinese and Latin text detection. We modified one class of images by adding specific watermarks while leaving the other class unchanged. We used a baseline dataset of 998 ImageNet images [†] to create 2 probing datasets (Chinese and Latin) by inserting random textual watermarks, as shown in Figure 12. For the Chinese-characters detection problem, the watermarks were generated by randomly selecting 7 out of the 20 most commonly used Chinese characters Da (2004), and a similar process was followed using the English alphabet for the Latin text detection problem. The font size for all watermarks has been set to 30, while the image dimensions remain standard at 224 × 224 pixels. AUC ROC was used as the performance metric to evaluate the representations' ability to differentiate between watermarked and normal classes. The true labels provided by the two datasets were used, where class 1 represents images with a watermark and class 0 represents images without. We computed the scalar activations for all images from both classes for a specific neural representation and then calculated the AUC ROC classification score based on the differences in activations using the binary labels. A score of 1 indicates a perfect classifier, consistently ranking watermarked images higher than normal ones, while a score of 0.5 indicates a random classifier.

A.3.2 ImageNet ResNet18

In the following, we provide additional details on the ResNet18 He et al. (2016) experiment, discussed in the main paper. The model was downloaded from the Torchvision library Marcel and Rodriguez (2010) and s-AMS were generated with parameters $n = 5$ and $m = 500$ using the `DORA` package.

Figure 13 illustrates the cluster of reported representations in the average pooling layer of the model, specifically neurons 154, 129, 347, 489, 81, 439, and 282, along with the sensitivity of other neurons to Chinese watermarks. It can be seen that representations close to the reported cluster also exhibit sensitivity towards malicious concepts. For additional context, Figure 18 shows the natural Activation-Maximisation signals (n-AMS) for the reported representations, obtained using 1 million subsamples of the ImageNet 2012 train dataset. The presence of Chinese watermarks in the n-AMS further supports our hypothesis of the Clever-Hans nature of these representations.

To examine which output class logits may be compromised by CH behavior, we used the s-AMS of the reported neurons to obtain class predictions on these signals. Figure 20 shows several s-AMS for the reported representations along with the network's predictions for the corresponding data points. We observed that certain classes, such as "carton" (478), "apron" (411), "swab, swob, mop" (840), "monitor" (664), and "broom" (462) were frequently predicted with high scores. When we computed the s-AMS for selected output logits, we found similar Chinese patterns, similar to those observed in the reported neurons of the average pooling layer (see Figure 20). These results suggest that such artifacts learned by the network pose a potential threat to applications due to the network's tendency to classify images with added watermarks as belonging to one of these classes.

A.3.3 DenseNet 121

The DORA framework was employed to investigate the pre-trained DenseNet121 on the ImageNet dataset Huang et al. (2017). Specifically, attention was focused on the last layer of the feature extractor, which comprised 1024 channel representations. The study primarily examined two outliers detected by DORA: neuron 768 and neuron 427, along with some of their nearest neighbors in the EA distance. Following an analysis of the s-AMS for both neurons, specific symbolic patterns were observed, which were characteristic of character detectors. Neuron 768 was identified as a Chinese-character detector, while neuron 427 was identified as a Latin text detector. Figure 9 in the main paper and Figure 14 depict these neurons, along with their closest neighbors in EA distance, which exhibited similar properties. The hypothesis was further supported by visualizing the n-AMS across the ImageNet dataset, as demonstrated in Figure 15.

As mentioned in Section 4.4.2, we find that the outliers found by DORA are maintained during fine-tuning on another dataset, e.g. the CheXpert challenge. The CheXpert challenge benchmarks various deep learning models on the task of classifying multilabel chest radiographs and additionally provides human experts, e.g.

[†] Images were obtained from `https://github.com/EliSchwartz/imagenet-sample-images`, with the exception of two images (of the class "carton" and "terrapin") that already exhibit watermarks.

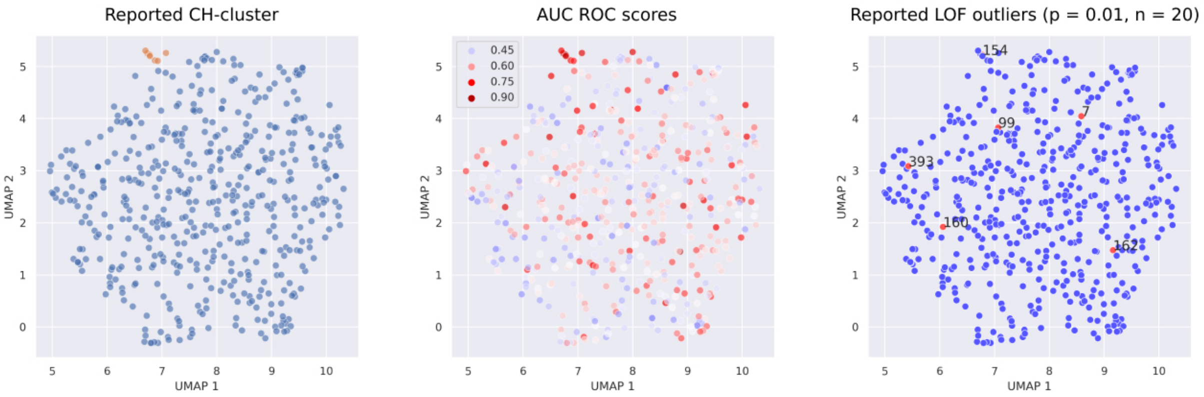

Figure 13: **Detailed illustration of the cluster of malicious representations found.** All of the figures illustrate the representation atlas of the average pooling layer of ResNet18, calculated using the DORA distance metric. From left to right: illustration of the reported Chinese detector cluster, the sensitivity of different representations for detecting Chinese watermarks, and a set of reported outliers among the representations using the LOF method. From the middle figure, it can be observed that the cluster of reported representations exhibits high sensitivity towards the artifactual concept of the desired task, and the closer the representations are to the cluster in the representation atlas, the more they are able to detect malicious concepts in the data.

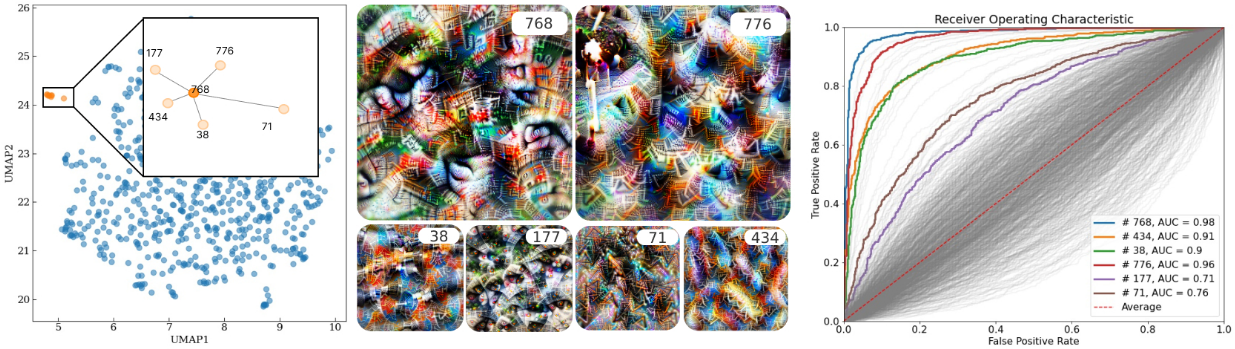

Figure 14: **DenseNet121 — Chinese-characters detector.** Applying DORA to the last layer of the feature extractor of DenseNet121 yields, among others, Neuron 768, which corresponds to the upper left of the 6 feature visualizations. From Neuron 768 as well as from its five closest neighbors (shown left), we can observe semantic concepts resembling Chinese logograms. The AUC values were computed using the channel activations on a data set that was corrupted with watermarks written in Chinese. As shown, the AUCs are high for the representation outliers found by DORA, compared to most of the other representations, which indicates that they indeed learned to detect Chinese logograms.

radiologists, with performance metrics for comparison. The data set itself consists of 224,316 training, 200 validation, and 500 test data points. The current best approach in terms of AUC-ROC score uses an ensemble of five DenseNet121's Huang et al. (2017) that were pre-trained on the ImageNet dataset and fine-tuned by optimizing a special surrogate loss for the AUC-ROC score Yuan et al. (2021). The training code can be found in this public repository `https://github.com/Optimization-AI/LibAUC/`. We choose to finetune one DenseNet121 using this approach on a downsampled version of the CheXpert data with a resolution of 256x256x3. The converged model yields an AUC-ROC score of 87.93% on the validation dataset. Having the finetuned DenseNet121 and the outlier neuron 768 at hand we show the Feature Visualizations and

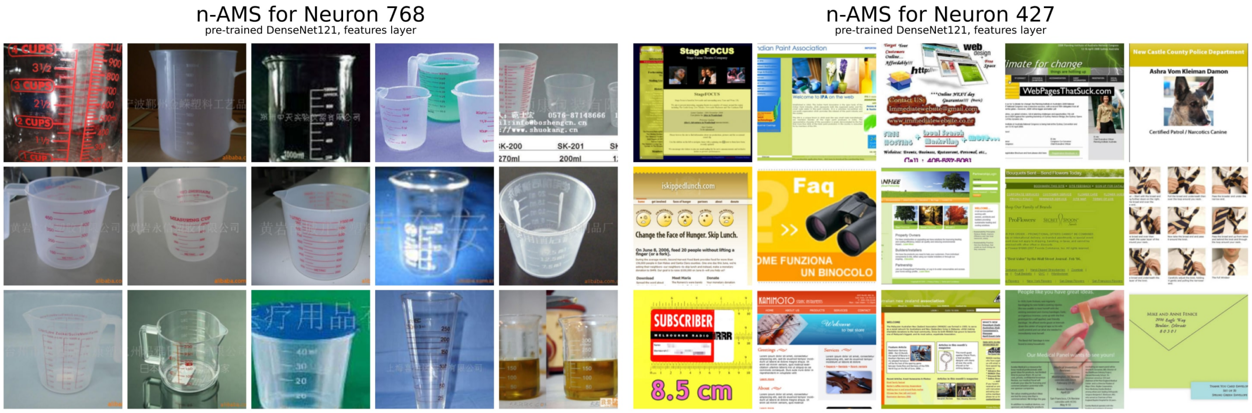
n-AMS for Neuron 768
pre-trained DenseNet121, features layer
n-AMS for Neuron 427
pre-trained DenseNet121, features layer

(a) Neuron 768

(b) Neuron 427

Figure 15: **n-AMS for different DenseNet121 neurons.** Illustration of the 15 n-AMS signals for the Chinse watermark detector (neuron 768) and the Latin text detector(neuron 427) in the "features" layer of DenseNet121.

the AUC-ROC curves for both the pre-trained and fine-tuned channel on an ImageNet subset with both uncorrupted and corrupted images with Chinese watermarks in Figure 16.

A.3.4 CLIP ResNet 50

The s-AMS for the CLIP ResNet 50 was computed using the same parameters as Goh et al. (2021) with the Lucent library. The number of optimization steps m was set to 512. The analysis was conducted on representations (channels) from the "layer 4" layer of the model. (Details on the s-AMS generation parameters can be found at `https://github.com/openai/CLIP-featurevis` and Lucent library at `https://github.com/greentfrapp/lucent`)

Star Wars representation

Figure 1 shows the limitations of the n-AMS approach when the data corpus for analysis differs from the training dataset. Figure 21 further illustrates n-AMS collected from ImageNet and Yahoo Creative Commons Thomee et al. (2016) datasets via `OpenAI Microscope`. Text Feature Visualization Goh et al. (2021) supports our hypothesis that the model is a detector of Star Wars-related concepts.

Outlier representations

Analysis of the representations space of the CIP model yielded a number of potential candidates to be considered outlier representations, namely neurons 631, 658, 838, 1666, 1865, and 1896. In Figure 22 we illustrate 3 s-AMS signals, alongside n-AMS images, collected from the ImageNet dataset per each reported representation, collected using `OpenAI Microscope`. While it is hard to explain the anomalous nature of neurons 631, 658, 838, 1666, and 1896, we can clearly observe how different the concept of neuron 1865 is.

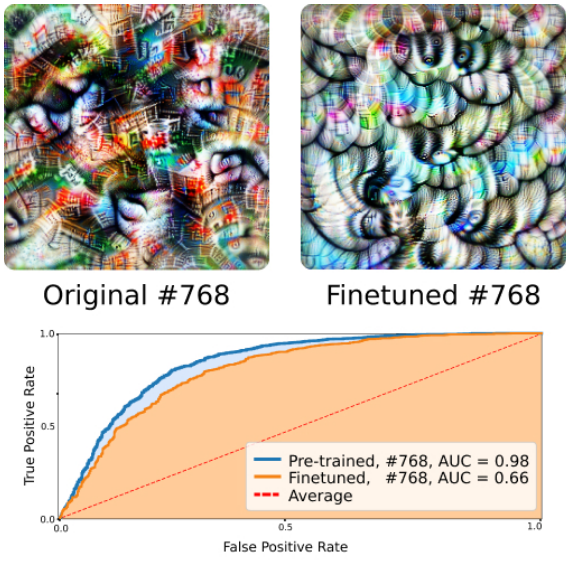

Figure 16: **Survived Chinese-characters detector**. Neuron 768 learns to detect Chinese logographic symbols during pre-training (top left) and does not unlearn this behavior during fine-tuning on the CheXpert dataset (top right). The AUC values of the neurons' activation on images corrupted with Chinese watermarks are still high after pre-training.

Table 3: **Clusters of CLIP “layer4” representations.** This table presents several interesting clusters and the indexes of the corresponding representations that were examined through manual inspection of the natural and synthetic AMS.

Cluster	*Representations*
Explicit/Pornographic	95, 255, 996, 1502, 2011
Money/Finance	785, 1376, 1731
Reptiles	230, 250, 417, 521, 652, 654, 694, 1008, 1234, 1301, 1340, 1364, 1445, 1598
Fish/Aquarium	1193, 1384
Asia-geographic	13,165, 235, 536, 780, 931, 1037, 1261, 1247,1423, 1669,1761,1874, 1898

Clsuters of representations

We manually examined several distinctive classes of representations in "layer 4" of the CLIP model after computing the representation atlas for the channel representations. Table 3 summarizes the results of our analysis and shows interesting clusters found along with the associated neurons. Figure 23 shows synthetic and natural AMS, providing evidence for the assignment of neurons to their respective clusters.

A.4 Experimental setup

All described experiments, if not stated otherwise, were performed on the Google Colab Pro Bisong and Bisong (2019) environment with the GPU accelerator.

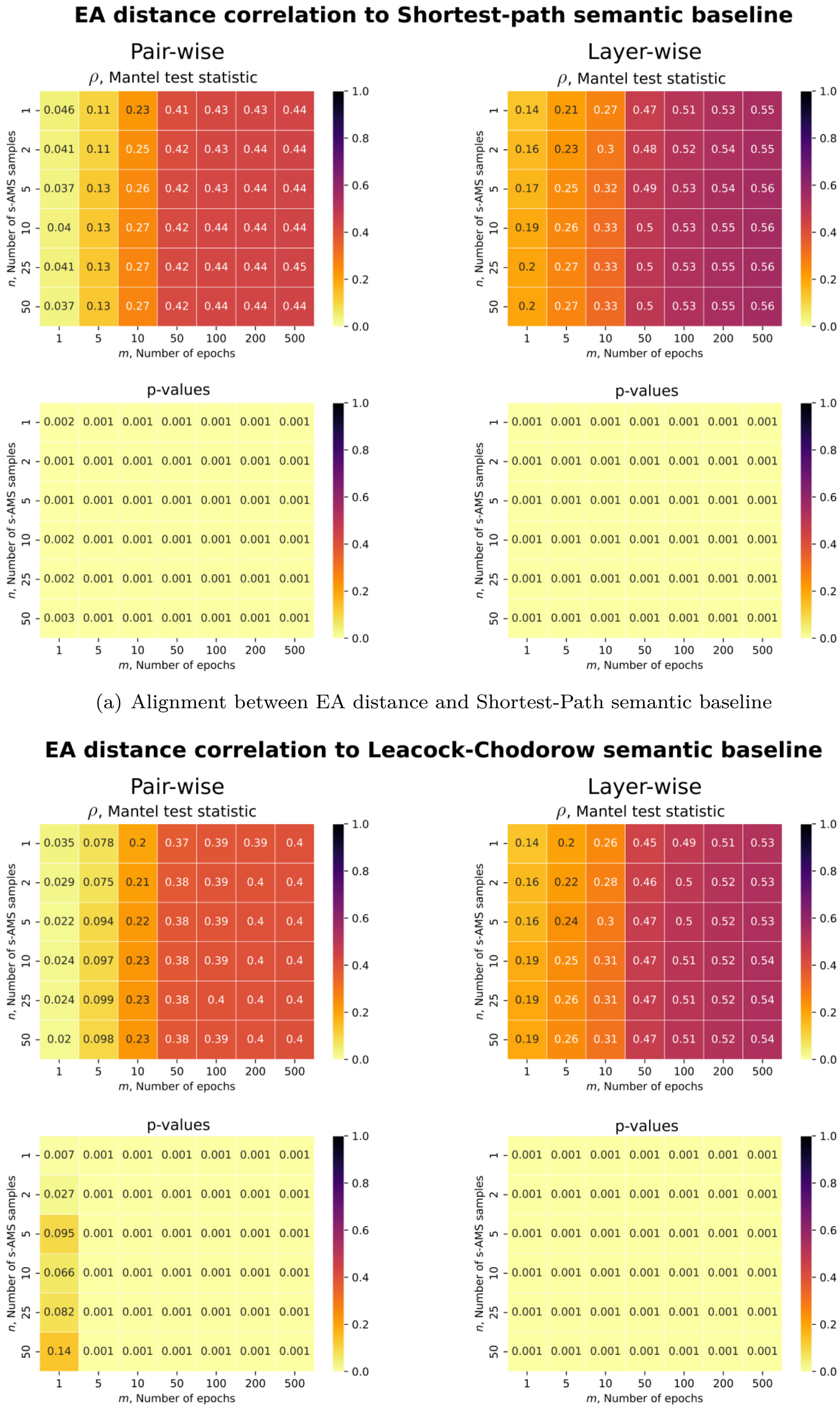

(a) Alignment between EA distance and Shortest-Path semantic baseline

(b) Alignment between EA distance and Leacock-Chodorow semantic baseline

Figure 17: **Mantel test statistics with corresponding p-values for comparison with Shortest-Path and Leacock-Chodorow distance.** The Mantel test was used to compare the EA distance matrices, varying parameters n and m (computed for the logit-output of an ImageNet pre-trained ResNet18 model), and the a) Shortest-Path and b) Leacock-Chodorow distance baseline (obtained from the WordNet taxonomy). The top row of the table shows the value of Mantel's ρ, which is a measure of the correlation between the two distance matrices. The bottom rows show the corresponding p-values, which indicate the statistical significance of the correlation.

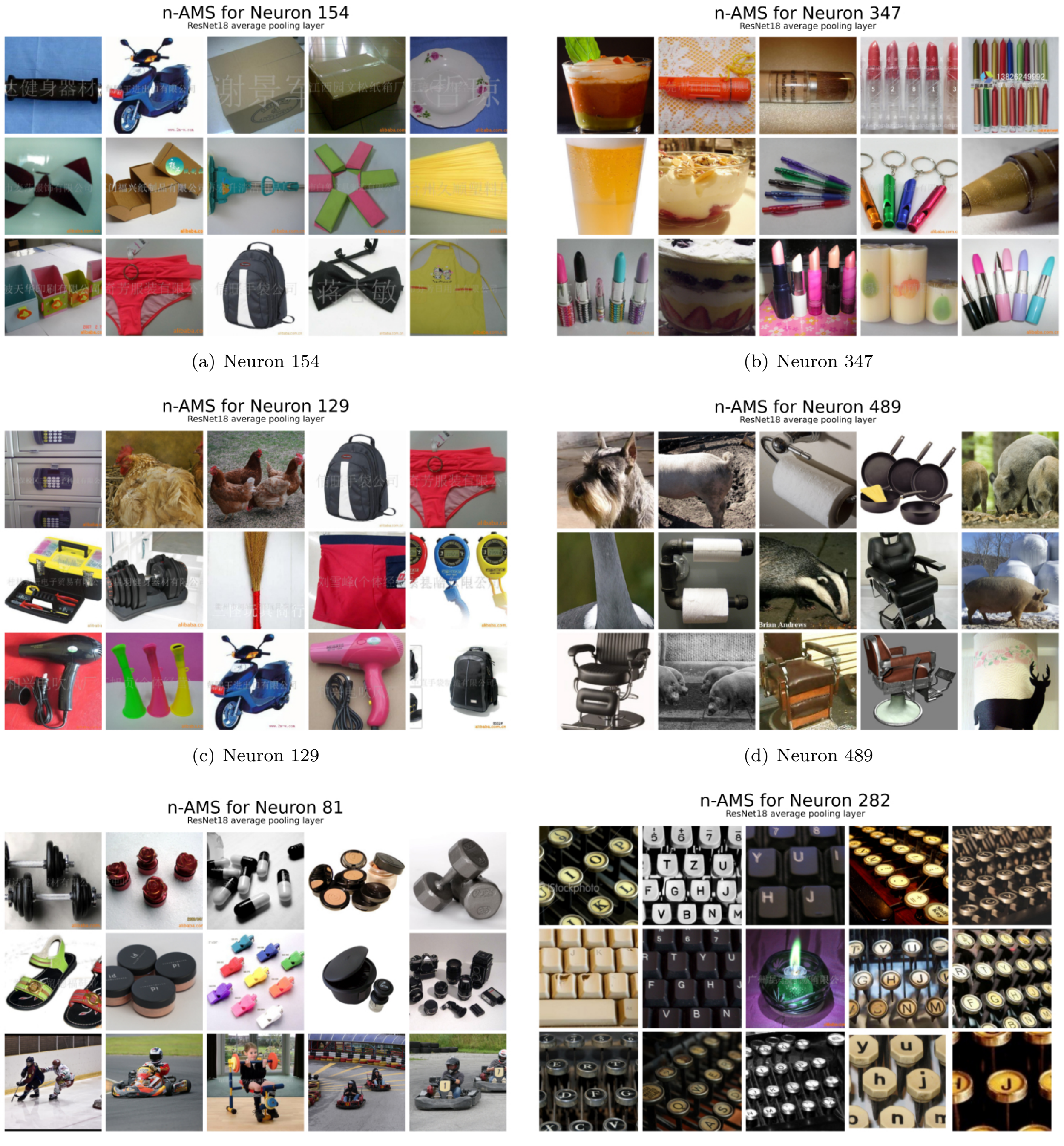
n-AMS for Neuron 154
ResNet18 average pooling layer
n-AMS for Neuron 347
ResNet18 average pooling layer
n-AMS for Neuron 129
ResNet18 average pooling layer
n-AMS for Neuron 489
ResNet18 average pooling layer
n-AMS for Neuron 81
ResNet18 average pooling layer
n-AMS for Neuron 282
ResNet18 average pooling layer

(a) Neuron 154

(b) Neuron 347

(c) Neuron 129

(d) Neuron 489

(e) Neuron 81

(f) Neuron 282

Figure 18: **n-AMS for different ResNet18 neurons, reported in the cluster of malicious representations.** The figure shows the 15 n-AMS signals for various neurons in the "avgpool" layer of the ResNet18 network, which were identified as being in the cluster of malicious representations. The signals were calculated using a subset of 1 million images from the ImageNet 2012 training dataset. It can be observed that among the top natural activation maximization signals, there are images of Chinese watermarks, supporting the hypothesis that these neurons have learned undesirable concepts.

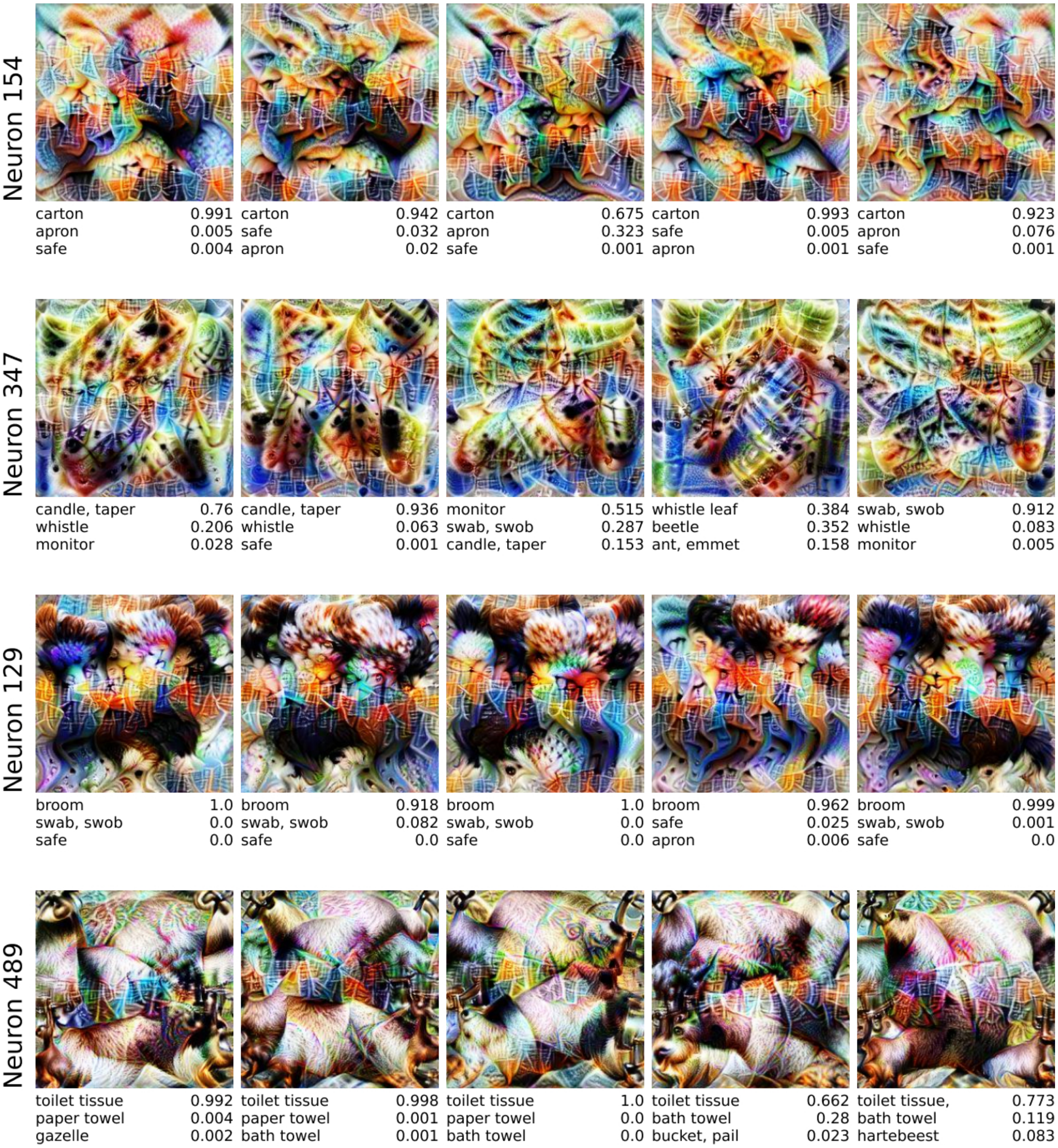

Figure 19: **s-AMS and model predictions for reported neurons in ResNet18.** Figure illustrates the s-AMS signals for four different reported neurons in the average pooling layer of ImageNet-trained ResNet18, along with the model's predictions for the top three classes with their respective softmax scores.

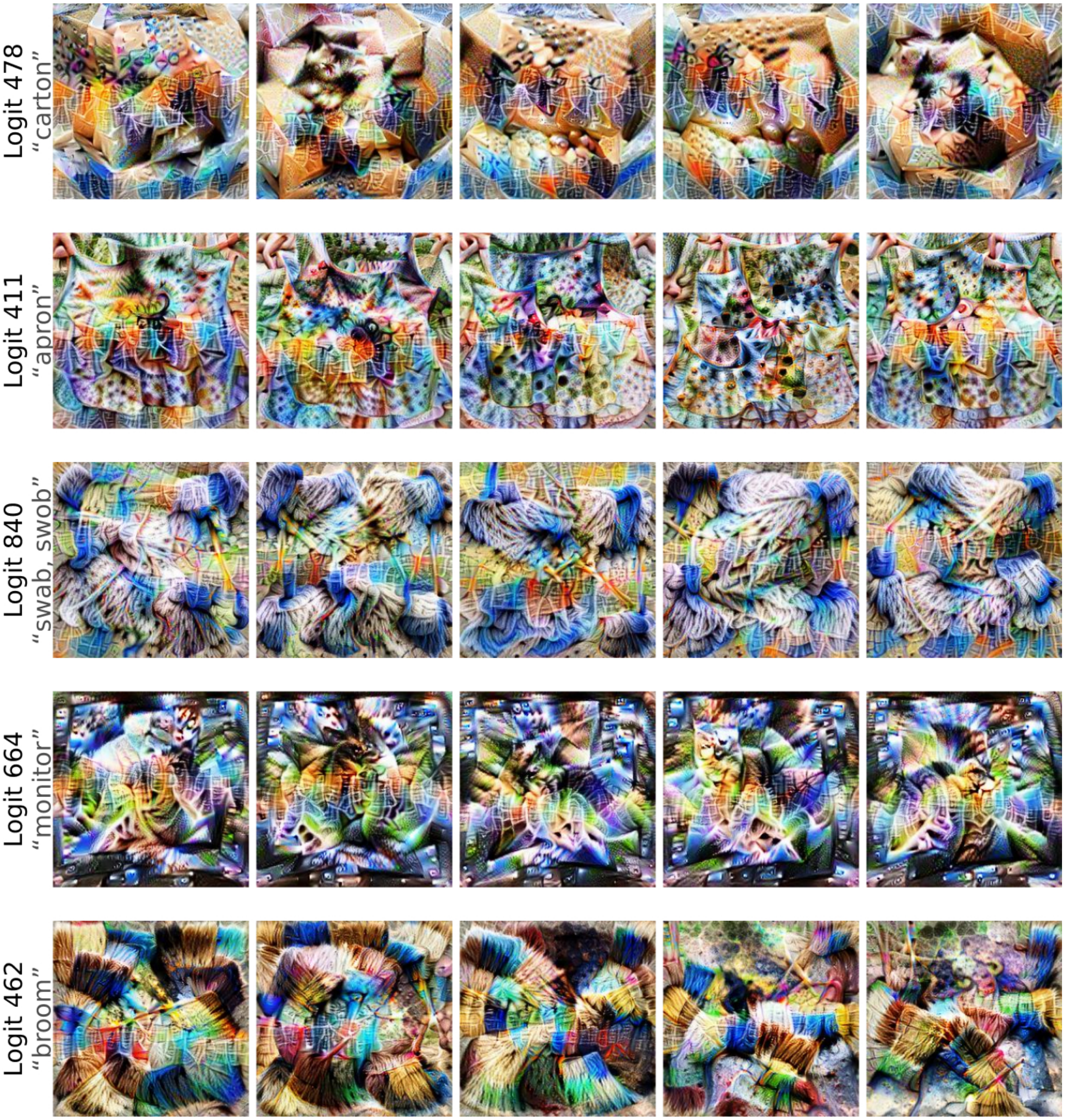

Figure 20: **s-AMS for several ResNet18 logits.** Figure shows s-AMS for the output logit representations of ResNet18. Similar to the reported neurons from the average pooling layer, the logits display logographic patterns, logographic patterns specific to Chinese character detectors, suggesting that these classes may be particularly affected by CH behavior.

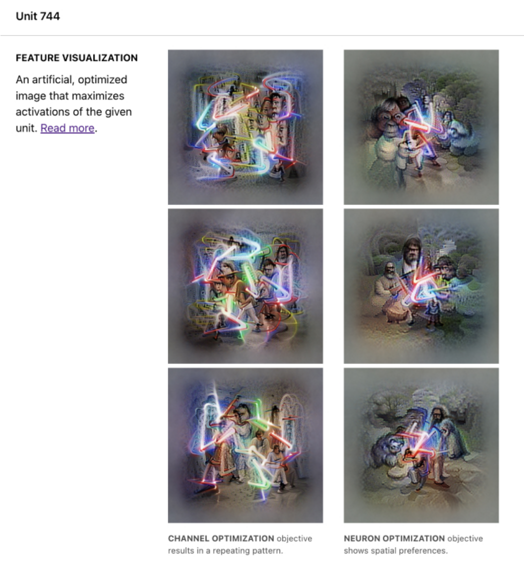

Unit 744

FEATURE VISUALIZATION

An artificial, optimized image that maximizes activations of the given unit. Read more.

CHANNEL OPTIMIZATION objective results in a repeating pattern.

NEURON OPTIMIZATION objective shows spatial preferences.

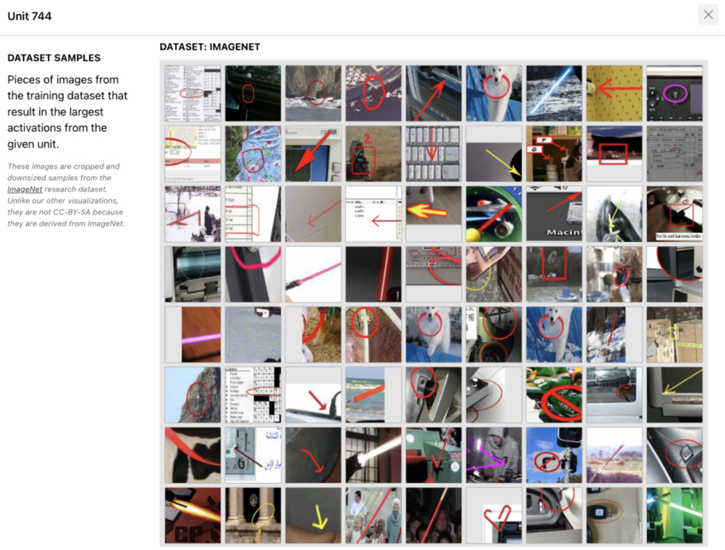

Unit 744

DATASET SAMPLES

Pieces of images from the training dataset that result in the largest activations from the given unit.

These images are cropped and downsized samples from the ImageNet research dataset. Unlike our other visualizations, they are not CC-BY-SA because they are derived from ImageNet.

DATASET: IMAGENET

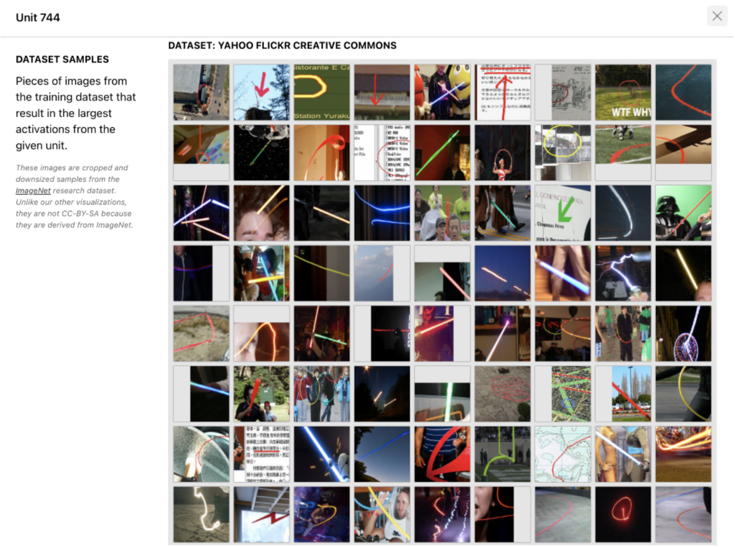

Unit 744

DATASET SAMPLES

Pieces of images from the training dataset that result in the largest activations from the given unit.

These images are cropped and downsized samples from the ImageNet research dataset. Unlike our other visualizations, they are not CC-BY-SA because they are derived from ImageNet.

DATASET: YAHOO FLICKR CREATIVE COMMONS

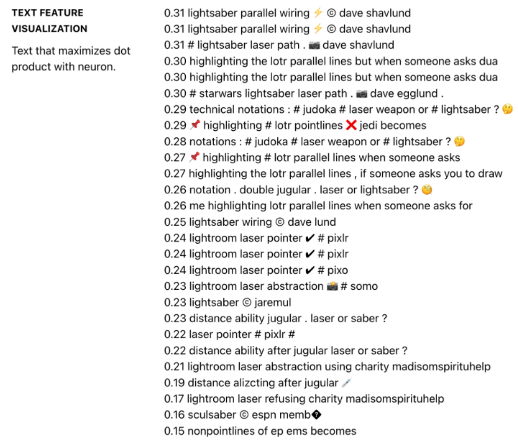

TEXT FEATURE VISUALIZATION

Text that maximizes dot product with neuron.

```
0.31 lightsaber parallel wiring ⚡ © dave shavlund
0.31 lightsaber parallel wiring ⚡ © dave shavlund
0.31 # lightsaber laser path . 📷 dave shavlund
0.30 highlighting the lotr parallel lines but when someone asks dua
0.30 highlighting the lotr parallel lines but when someone asks dua
0.30 # starwars lightsaber laser path . 📷 dave egglund .
0.29 technical notations : # judoka # laser weapon or # lightsaber ? 🤔
0.29 📌 highlighting # lotr pointlines ❌ jedi becomes
0.28 notations : # judoka # laser weapon or # lightsaber ? 🤔
0.27 📌 highlighting # lotr parallel lines when someone asks
0.27 highlighting the lotr parallel lines , if someone asks you to draw
0.26 notation . double jugular . laser or lightsaber ? 🧐
0.26 me highlighting lotr parallel lines when someone asks for
0.25 lightsaber wiring © dave lund
0.24 lightroom laser pointer ✔ # pixlr
0.24 lightroom laser pointer ✔ # pixlr
0.24 lightroom laser pointer ✔ # pixo
0.23 lightroom laser abstraction 📸 # somo
0.23 lightsaber © jaremul
0.23 distance ability jugular . laser or saber ?
0.22 laser pointer # pixlr #
0.22 distance ability after jugular laser or saber ?
0.21 lightroom laser abstraction using charity madisomspirituhelp
0.19 distance alizcting after jugular 💉
0.17 lightroom laser refusing charity madisomspirituhelp
0.16 sculsaber © espn memb�
0.15 nonpointlines of ep ems becomes
```

Figure 21: **CLIP ResNet Neuron 744.** The figure shows s-AMS and n-AMS for neuron 744 in the "layer 4" layer of the model, computed for 2 different data corpora. The observed signals and explanations from Text Feature Visualization confirm that the neuron can detect Star Wars-related concepts. Results obtained from `OpenAI Microscope`.

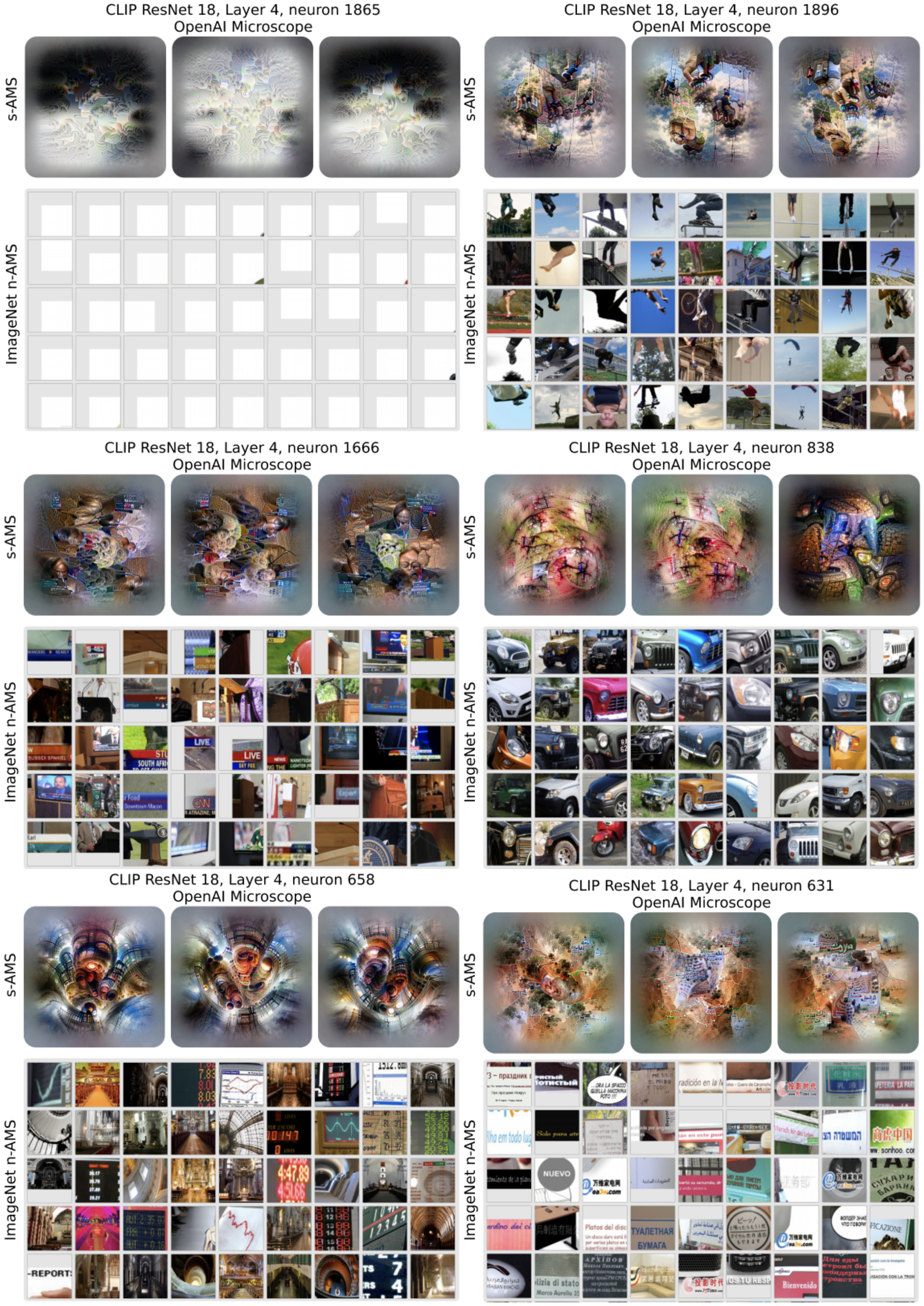

Figure 22: **s-AMS and n-AMS for reported outlier neurons.** Figure illustrates s-AMS and n-AMS for the reported outlier neurons in the "layer 4" layer of the CLIP ResNet 50 model, collected from `OpenAI Microscope`.

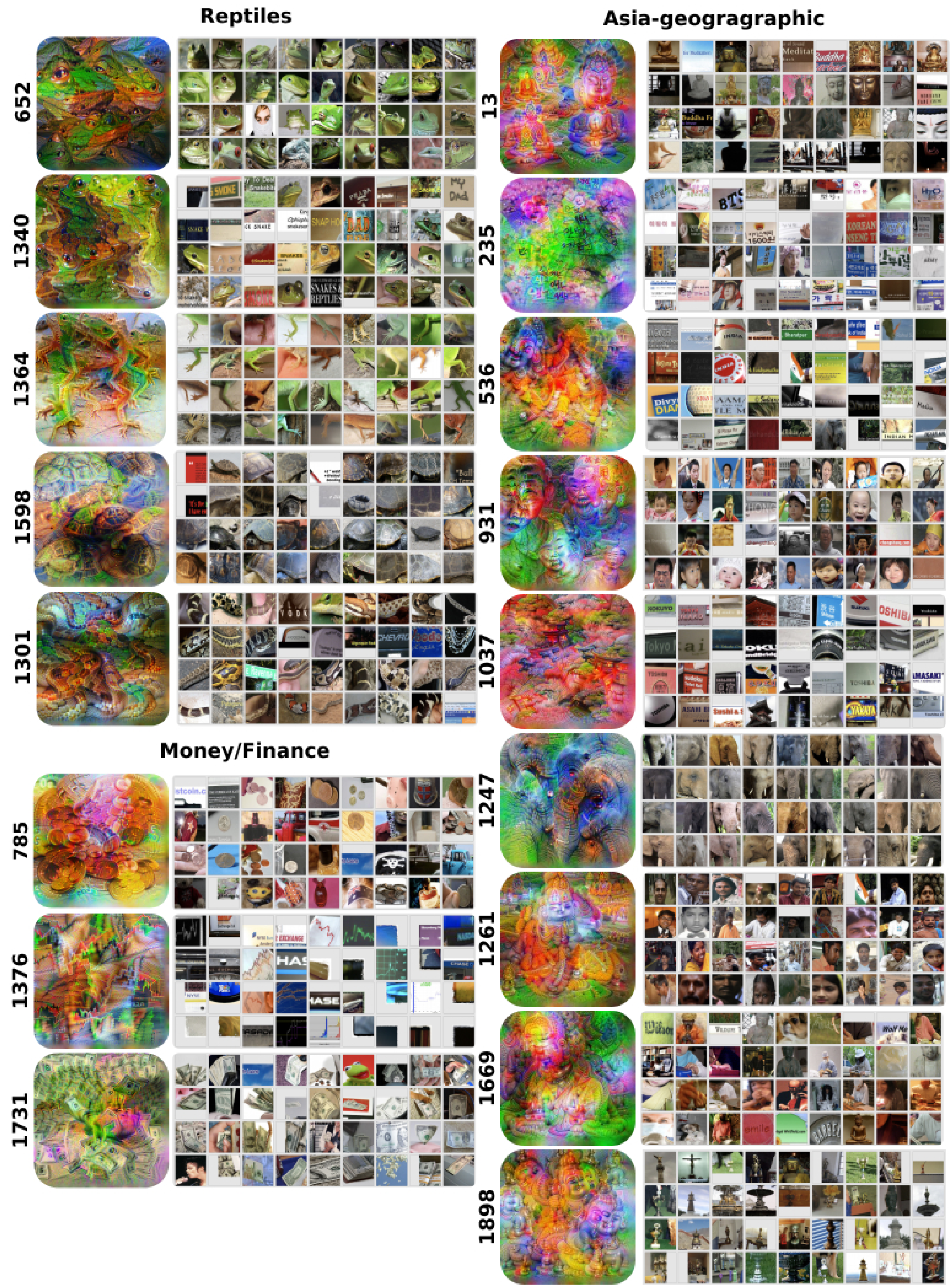

Figure 23: **s-AMS and n-AMS for the neurons in the reported clusters.** Figure shows s-AMS and n-AMS for representations assigned to different reported clusters. s-AMS were generated, while n-AMS (Activation-Maximization images from ImageNet dataset) were collected via `OpenAI Microscope`. Representations of explicit/pornographic content were excluded due to the presence of obscene images.